

Riemannian Multi-Manifold Modeling

Xu Wang¹, Konstantinos Slavakis², and Gilad Lerman¹

¹Dept. of Mathematics, University of Minnesota, Minneapolis, MN 55455, USA
{wang1591,lerman}@umn.edu

²Dept. of Electrical & Computer Eng. and Digital Technology Center,
University of Minnesota, Minneapolis, MN 55455, USA
kslavaki@umn.edu

Abstract

This paper advocates a novel framework for segmenting a dataset in a Riemannian manifold M into clusters lying around low-dimensional submanifolds of M . Important examples of M , for which the proposed clustering algorithm is computationally efficient, are the sphere, the set of positive definite matrices, and the Grassmannian. The clustering problem with these examples of M is already useful for numerous application domains such as action identification in video sequences, dynamic texture clustering, brain fiber segmentation in medical imaging, and clustering of deformed images. The proposed clustering algorithm constructs a data-affinity matrix by thoroughly exploiting the intrinsic geometry and then applies spectral clustering. The intrinsic local geometry is encoded by local sparse coding and more importantly by directional information of local tangent spaces and geodesics. Theoretical guarantees are established for a simplified variant of the algorithm even when the clusters intersect. To avoid complication, these guarantees assume that the underlying submanifolds are geodesic. Extensive validation on synthetic and real data demonstrates the resiliency of the proposed method against deviations from the theoretical model as well as its superior performance over state-of-the-art techniques.

1 Introduction

Many modern data sets are of moderate or high dimension, but manifest intrinsically low-dimensional structures. A natural quantitative framework for studying such common data sets is multi-manifold modeling (MMM) or its special case of hybrid-linear modeling (HLM). In this MMM framework a given dataset is modeled as a union of submanifolds (whereas HLM considers union of subspaces). When proposing a valid algorithm for MMM, one assumes an underlying dataset that can be modeled as mixture of submanifolds and tries to prove under some conditions that the proposed algorithm can cluster the dataset according to the submanifolds. This framework has been extensively studied and applied for datasets embedded in the Euclidean space or the sphere (Arias-Castro et al., 2011; Arias-Castro et al., 2013; Cetingul and Vidal, 2009; Elhamifar and Vidal, 2011; Kushnir et al., 2006; Ho et al., 2013a; Lui, 2012; Wang et al., 2011).

Nevertheless, there is an overwhelming number of application domains, where information is extracted from datasets that lie on Riemannian manifolds, such as the Grassmannian, the sphere, the orthogonal group, or the manifold of symmetric positive (semi)definite [P(S)D] matrices. For example, auto-regressive moving average (ARMA) models are utilized to extract low-rank linear subspaces (points on the Grassmannian) for identifying spatio-temporal dynamics in video sequences (Turaga et al., 2011). Similarly, convolving patches of images by Gabor filters yields covariance matrices (points on the PD manifold) that can capture effectively texture patterns in images (Tou et al., 2009). Nevertheless, current MMM strategies are not sufficiently accurate for handling data in more general Riemannian spaces.

The purpose of this paper is to develop theory and algorithms for the MMM problem in more general Riemannian spaces that are relevant to important applications.

Related Work. Recent advances in parsimonious data representations and their important implications in dimensionality reduction techniques have effected the development of non-standard spectral-clustering schemes that result in state-of-the-art results in modern applications (Arias-Castro et al., 2013; Chen and Lerman, 2009a; Elhamifar and Vidal, 2009; Goh and Vidal, 2008; Goldberg et al., 2009; Harandi et al., 2013; Liu et al., 2013; Zhang et al., 2012). Such schemes rely on the assumption that data exhibit low-dimensional structures, such as unions of low-dimensional linear subspaces or submanifolds embedded in Euclidean spaces.

Several algorithms for clustering on manifolds are generalizations of well-known schemes developed originally for Euclidean spaces. For example, Gruber and Theis (2006) extended the classical K -means algorithm from Euclidean spaces to Grassmannians, and illustrated an application to nonnegative matrix factorization. Tuzel et al. (2005) capitalized on the Riemannian distance of $SO(3)$ to design an efficient mean-shift (MS) algorithm for multiple 3D rigid motion estimation. Subbarao and Meer (2006), as well as Cetingul and Vidal (2009), extended further the MS algorithm to general analytic manifolds including Grassmannians, Stiefel manifolds, and matrix Lie groups. O’Hara et al. (2011) showed promising results by using the geodesic distance of product manifolds in clustering of human expressions, gestures, and actions in videos. Rathi et al. (2007) solved the image segmentation problem, after recasting it as a matrix clustering problem, via probability distributions on symmetric PD matrices. Goh and Vidal (2008) extended spectral clustering and nonlinear dimensionality reduction techniques to Riemannian manifolds. These previous works are quite successful when the convex hulls of individual clusters are well-separated, but they often fail when clusters intersect or are closely located.

HLM and MMM accommodate low-dimensional data structures by unions of subspaces or submanifolds, respectively, but are restricted to manifolds embedded in either a Euclidean space or the sphere. Many strategies have been suggested for solving the HLM problem, known also as subspace clustering. These strategies include methods inspired by energy minimization (Bradley and Mangasarian, 2000; Ho et al., 2003; Ma et al., 2007; Poling and Lerman, 2014; Tseng, 2000; Zhang et al., 2009, 2010), algebraic methods (Boult and Brown, 1991; Costeira and Kanade, 1998; Kanatani, 2001, 2002; Ma et al., 2008; Ozay et al., 2010; Vidal et al., 2005), statistical methods (Tipping and Bishop, 1999; Yang et al., 2006), and spectral-type methods with various types of affinities representing subspace-related information (Chen and Lerman, 2009a; Elhamifar and Vidal, 2013; Liu et al., 2013; Yan and Pollefeys, 2006; Zhang et al., 2012). Recent tutorial papers on HLM are Vidal (2011) and Aldroubi (2013). Some theoretical guarantees for particular HLM algorithms appear in (Chen and Lerman, 2009b; Lerman and Zhang, 2011; Soltanolkotabi and Candès, 2012; Soltanolkotabi et al., 2014). There are fewer strategies for the MMM problem, which is also known as manifold clustering. They include higher-order spectral clustering (Arias-Castro et al., 2011), spectral methods based on local PCA (Arias-Castro et al., 2013; Goldberg et al., 2009; Gong et al., 2012; Kushnir et al., 2006; Wang et al., 2011), sparse-coding-based spectral clustering in a Euclidean space (Elhamifar and Vidal, 2011) and its modification to the sphere by Cetingul et al. (2014) (the sparse coding encodes local subspace approximation), energy minimization strategies (Guo et al., 2007), methods based on manifold learning algorithms (Polito and Perona, 2001; Souvenir and Pless, 2005), and methods based on clustering dimension or local density (Barbará and Chen, 2000; Gionis et al., 2005; Haro et al., 2006). Notwithstanding, only higher-order spectral clustering and spectral local PCA are theoretically guaranteed (Arias-Castro et al., 2011; Arias-Castro et al., 2013).

In a different context, Rahman et al. (2005) suggested multiscale strategies for signals taking values in Riemannian manifolds, in particular, the sphere, the orthogonal group, the Grassmannian, and the PD manifold. Even though Rahman et al. (2005) addresses a completely different problem, its basic principle is similar in spirit to ours and can be described as follows. Local analysis is performed in the tangent

spaces, where the exponential and logarithm maps are used to transform data between local manifold neighborhoods and local tangent space neighborhoods. Information from all local neighborhoods is then integrated to infer global properties.

Contributions. Despite the popularity of manifold learning, the associated literature lacks generic schemes for clustering low-dimensional data embedded in non-Euclidean spaces. Furthermore, even in the Euclidean setting only few algorithms for MMM or HLM are theoretically guaranteed. To this end, this paper aims at filling this gap and provides an MMM approach in non-Euclidean setting with some theoretical guarantees even when the clusters intersect. In order to avoid nontrivial theoretical obstacles, the theory assumes that the underlying submanifolds are geodesic and refer to it as *multi-geodesic modeling* (MGM). Clearly, this modeling paradigm is a direct generalization of HLM from Euclidean spaces to Riemannian manifolds. A more practical and robust variant of the theoretical algorithm is also developed, and its superior performance over state-of-the-art clustering techniques is exhibited by extensive validation on synthetic and real datasets. We remark that in practice we require that the logarithm map of M can be computed efficiently and we show that this assumption does not restrict the wide applicability of this work.

We believe that it is possible to extend the theoretical foundations of this work to deal with general submanifolds by using local geodesic submanifolds (in analogy to Arias-Castro et al. (2013)). However, this will significantly increase the complexity of our proof, which is already not simple. Nevertheless, the proposed method directly applies to the more general setting (without theoretical guarantees) since geodesics are only used in local neighborhoods and not globally. Furthermore, our numerical experiments show that the proposed method works well in real practical scenarios that deviate from the theoretical model.

On a more technical level, the paper is distinguished from previous works in multi-manifold modeling in its careful incorporation of “directional information,” e.g., local tangent spaces and geodesics. This is done for two purposes: (i) To distinguish submanifolds at intersections; (ii) to filter out neighboring points that belong to clusters different than the cluster of the query point. In such a way, the proposed algorithm allows for neighborhoods to include points from different clusters, while previous multi-manifold algorithms (e.g., Elhamifar and Vidal (2011)) need careful choice of neighborhood radii to avoid points belonging to other clusters.

2 Theoretical Preliminaries

We formulate the theoretical problem of MGM and review preliminary background of Riemannian geometry, which is necessary to follow this work.

2.1 Multi-Geodesic Modeling (MGM)

MGM assumes that each point in a given dataset $X = \{x_i\}_{i=1}^N$ lies in the tubular neighborhood of some unknown geodesic submanifold S_k , $1 \leq k \leq K$, of a Riemannian manifold, M .¹ The goal is to cluster the dataset X into K groups $X_1, \dots, X_K \subset M$ such that points in X_k are associated with the submanifold S_k . Note that if M is a Euclidean space, geodesic submanifolds are subspaces and MGM boils down to HLM, or equivalently, subspace clustering (Elhamifar and Vidal, 2009; Vidal, 2011; Zhang et al., 2012).

For theoretical purposes, we assume the following data model, which we refer to as uniform MGM: The data points are i.i.d. sampled w.r.t. the uniform distribution on a fixed tubular neighborhood of $\cup_{k=1}^K S_k$.

¹The tubular neighborhood with radius $\tau > 0$ of S_k in M (with metric tensor g and induced distance dist_g) is $S_k^\tau = \{x \in M : \text{dist}_g(x, s) < \tau \text{ for some } s \in S_k\}$.

We denote the radius of the tubular neighborhood by τ and refer to it as the noise level. Figure 1 illustrates data generated from uniform MGM with two underlying submanifolds ($K = 2$).

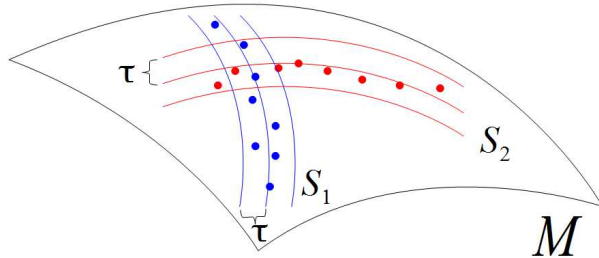


Figure 1: Illustration of data generated from a uniform MGM when $K = 2$.

The MGM problem only serves our theoretical justification. The numerical experiments show that the proposed algorithm works well under a more general MMM setting. Such a setting may include more general submanifolds (not necessarily geodesic), non-uniform sampling and different kinds and levels of noise.

2.2 Basics of Riemannian Geometry

This section reviews basic concepts from Riemannian geometry; for extended and accessible review of the topic we recommend the textbook by do Carmo (1992). Let (M, g) be a D -dimensional Riemannian manifold with a metric tensor g . A geodesic between $x, y \in M$ is a curve in M whose length is locally minimized among all curves connecting x and y . Let $\text{dist}_g(x, y)$ be the Riemannian distance between x and y on M . If $T_x M$ denotes the tangent space of M at x , then $T_x S$ stands for the tangent subspace of a d -dimensional geodesic submanifold S at x . As shown in Figure 2a, $T_x S$ is a linear subspace of $T_x M$. The exponential map \exp_x maps a tangent vector $\mathbf{v} \in T_x M$ to a point $\exp_x(\mathbf{v}) \in M$, which provides local coordinates around x . By definition, the geodesic submanifold S is the image of $T_x S$ under \exp_x (cf., Definition 2). The functional inverse of \exp_x is the logarithm map \log_x from M to $T_x M$, which maps x to the origin \mathbf{O} of $T_x M$. Let $\mathbf{x}_j^{(i)}$ denote the image of a data point x_j in $T_{x_i} M$ by the logarithm map at x_i ; that is, $\mathbf{x}_j^{(i)} = \log_{x_i}(x_j)$.

3 Solutions for the MGM (or MMM) Problem in M

We suggest solutions for the MMM problem in M with theoretical guarantees supporting one of these solutions when restricting the problem to MGM. Section 3.1 defines two key quantities for quantifying directional information: Estimated local tangent subspaces and geodesic angles. Section 3.2 presents the two solutions and discusses their properties.

3.1 Directional Information

The Estimated Local Tangent Subspace $T_{x_i}^E S$. Figure 2b demonstrates the main quantity defined here ($T_{x_i}^E S$) as well as related concepts and definitions. It assumes a dataset $X = \{x_j\}_{j=1}^N \subset M$ generated by uniform MGM with a single geodesic submanifold S . The dataset is thus contained in a tubular neighborhood of a d -dimensional geodesic submanifold S . Since S is geodesic, for any $1 \leq i \leq N$ the set $\{\mathbf{x}_j^{(i)}\}_{j=1}^N$ of images by the logarithm map is contained in a tubular neighborhood of the d -dimensional subspace $T_{x_i} S$ (possibly with a different radius than τ).

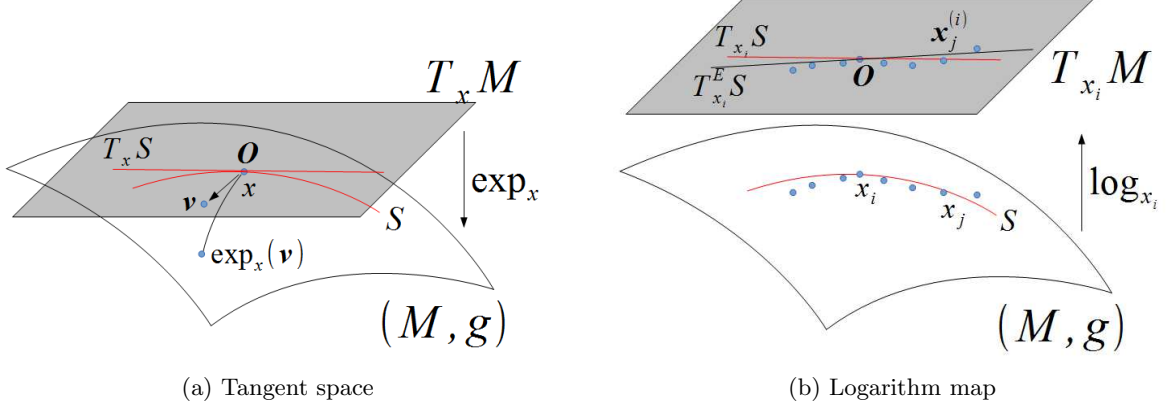


Figure 2: Demonstration of the exponential and logarithm maps as well as the tangent and estimated subspaces. (a) The tangent space and the exponential map of a manifold (M, g) at a point $x \in M$. Note that the tangent subspace $T_x S$ is a pre-image of S under the exponential map. (b) The logarithm map \log_{x_i} w.r.t. $x_i \in S$ and the images by \log_{x_i} of data points in a local neighborhood of x_i , in particular, $\mathbf{x}_j^{(i)}$, the image of x_j . Note the difference between $T_{x_i} S$, which is the image of S under \log_{x_i} , and the subspace $T_{x_i}^E S$ estimated by the images of the data points in the local neighborhood.

Since the true tangent subspace $T_{x_i} S$ is unknown, an estimation of it, $T_{x_i}^E S$, is needed. Let $B(x_i, r) \subset M$ be the neighborhood of x_i with a fixed radius $r > 0$. Let

$$J(x, r) := \{j : x_j \in B(x, r) \cap X\}. \quad (1)$$

Moreover, let \mathbf{C}_{x_j} denote the local sample covariance matrix of the dataset $\{\mathbf{x}_j^{(i)}\}_{j \in J(x_i, r)}$ on $T_{x_i} M$, and $\|\mathbf{C}_{x_j}\|$ the spectral norm of \mathbf{C}_{x_j} , i.e., its maximum eigenvalue. Since $\{\mathbf{x}_j^{(i)}\}_{j=1}^N$ is in a tubular neighborhood of a d -dimensional subspace, estimates of the intrinsic dimension d of the local tangent subspace, which is also the dimension of S , can be formed by bottom eigenvalues of \mathbf{C}_{x_j} (cf., Arias-Castro et al. (2013)). We adopt this strategy of dimension estimation and define the estimated local tangent subspace, $T_{x_i}^E S$, as the span in $T_{x_i} M$ of the top eigenvectors of \mathbf{C}_{x_j} . In theory, the number of top eigenvectors is the number of eigenvalues of \mathbf{C}_{x_i} that exceed $\eta \|\mathbf{C}_{x_j}\|$ for some fixed $0 < \eta < 1$ (see Theorem 1 and its proof for the choice of η). In practice, the number of top eigenvectors is the number of top eigenvalues \mathbf{C}_{x_i} until the largest gap occurs.

Empirical Geodesic Angles. Let $l(x_i, x_j)$ be the shortest geodesic (global length minimizer) connecting x_i and x_j in (M, g) . Let $\mathbf{v}_{ij} \in T_{x_i} M$ be the tangent vector of $l(x_i, x_j)$ at x_i . In other words, \mathbf{v}_{ij} shows the direction at x_i of the shortest path from x_i to x_j . Given a dataset $X = \{x_j\}_{j=1}^N$, the empirical geodesic angle θ_{ij} is the elevation angle (cf., (9) of Lerman and Whitehouse (2009)) between the vector \mathbf{v}_{ij} and the subspace $T_{x_i}^E S$ in the Euclidean space $T_{x_i} M$.

3.2 Proposed Solutions

In Section 3.2.1, we propose a theoretical solution for data sampled according to uniform MGM. We start with its basic motivation, then describe the proposed algorithm and at last formulate its theoretical guarantees. In Section 3.2.2, we propose a practical algorithm. At last, Section 3.2.3 discusses the numerical complexity of both algorithms.

3.2.1 Algorithm 1: Theoretical Geodesic Clustering with Tangent information (TGCT)

The proposed solution for the MGM-clustering task applies spectral clustering with carefully chosen weights. Specifically, a similarity graph is constructed whose vertices are data points and whose edges represent the similarity between data points. The challenge is to construct a graph such that two points are locally connected only when they come from the same cluster. This way spectral clustering will recover exactly the underlying clusters.

For the sake of illustration, let us assume only two underlying geodesic submanifolds S_1 and S_2 . We also assume that the data was sampled from $S_1 \cup S_2$ according to uniform MGM. Given a point $x_0 \in S_1$ one wishes to connect to it the points from the same submanifold within a local neighborhood $B(x_0, r)$ for some $r > 0$. Clearly, it is not realistic to assume that all points in $B(x_0, r)$ are from the same submanifold of x_0 (due to nearness and intersection of clusters as demonstrated in Figures 3a and 3b).

We first assume no intersection at x_0 as demonstrated in Figure 3a. In order to be able to identify the points in $B(x_0, r)$ from the same submanifold of x_0 , we use local tangent information at x_0 . If $x \in B(x_0, r)$ belongs to S_2 , then the geodesic $l(x_0, x)$ has a large angle with the tangent space $T_{x_0}S_1$ at x_0 . On the other hand, if such x belongs to S_1 , then the geodesic has an angle close to zero. Therefore, thresholding the empirical geodesic angles may become beneficial for eliminating neighboring points belonging to a different submanifold (cf., Figure 3a).

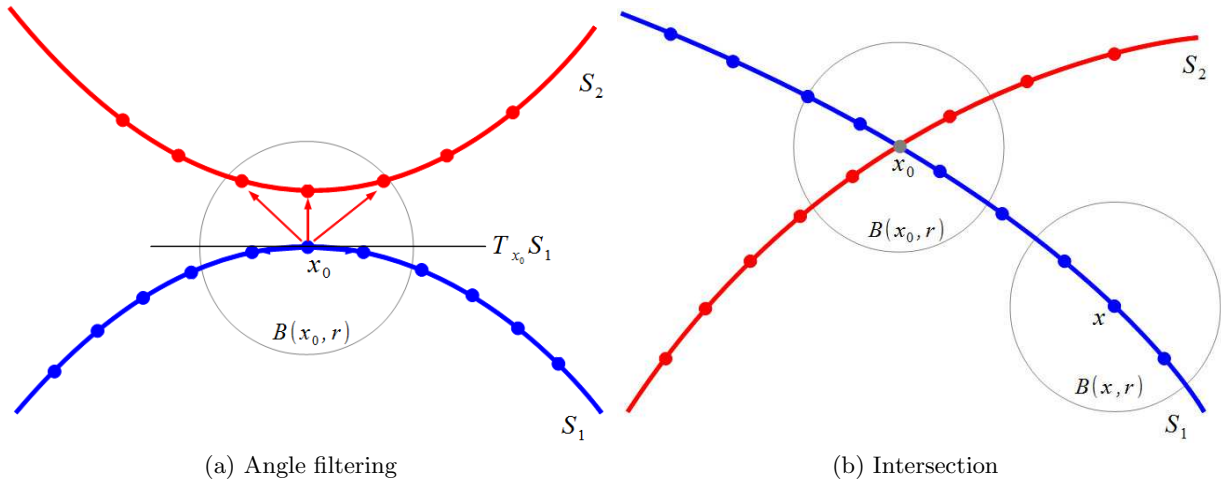


Figure 3: In Figures 3a and 3b, blue points lie on the submanifold S_1 and red points lie on the submanifold S_2 . In Figure 3a, a local neighborhood, which is a disk of radius r , around the blue point x_0 is observed and the goal is to exclude the red points in $B(x_0, r)$. This can be done by thresholding the angles between geodesics and the tangent subspace $T_{x_0}S_1$. Indeed, the angles w.r.t. blue points are close to zero and the angles w.r.t. red points are sufficiently large. In Figure 3b, a point x_0 is in $S_1 \cup S_2$ and an arbitrary point x sufficiently far from it. The goal is to assure that x is not connected to x_0 . This can be done by comparing local estimated dimensions. The estimated dimension in $B(x_0, r)$ is $\dim(S_1) + \dim(S_2)$, while the estimated dimension in $B(x, r)$ is $\dim(S_1)$. Due to the dimension difference, the intersection is disconnected from the two submanifolds.

If x_0 is at or near the intersection, it is hard to estimate correctly the tangent spaces of each submanifold and the geodesic angles may not be reliable. Instead, one may compare the dimensions of estimated local tangent subspaces. The estimated dimensions of local neighborhoods of data points, which are close to intersections, are larger than the estimated dimensions of local neighborhoods of data points further away from intersections (cf., Figure 3b). The algorithm thus connects x_0 to other neighboring points only when

their “local dimensions” (linear-algebraic dimension of the estimated local tangent) are the same. In this way, the intersection will not be connected with the other clusters.

The dimension difference criterion, together with the angle filtering procedure, guarantee that there is no false connection between different clusters (the rigorous argument is established in the proof of Theorem 1). We use these two simple ideas and the common spectral-clustering procedure to form the Theoretical Geodesic Clustering with Tangent information (TGCT) in Algorithm 1.

Algorithm 1 Theoretical Geodesic Clustering with Tangent information (TGCT)

Input: Number of clusters: $K \geq 2$, a dataset X of N points, a neighborhood radius r , a projection threshold η for estimating tangent subspaces, a distance threshold σ_d and an angle threshold σ_a .

Output: Index set $\{\text{Id}_i\}_{i=1}^N$ such that $\text{Id}_i \in \{1, \dots, K\}$ is the cluster label assigned to x_i

Steps:

- Compute the following geometric quantities around each point:

for $i = 1, \dots, N$ **do**

- For $j \in J(x_i, r)$ (c.f., (1)), compute $\mathbf{x}_j^{(i)} = \log_{x_i}(x_j)$
- Compute the sample covariance matrix \mathbf{C}_{x_i} of $\{\mathbf{x}_j^{(i)}\}_{j \in J(x_i, r)}$
- Compute the eigenvectors of \mathbf{C}_{x_i} whose eigenvalues exceed $\eta \cdot \|\mathbf{C}_{x_i}\|$ (their span is $T_{x_i}^E S$)
- For all $j = 1, \dots, N$, compute the empirical geodesic angles θ_{ij} (see Section 3.1)

end for

- Form the following $N \times N$ affinity matrix \mathbf{W} :

$$\mathbf{W}_{ij} = \mathbf{1}_{\text{dist}_g(x_i, x_j) < \sigma_d} \mathbf{1}_{\dim(T_{x_i}^E S) = \dim(T_{x_j}^E S)} \mathbf{1}_{(\theta_{ij} + \theta_{ji}) < \sigma_a}$$

- Apply spectral clustering to the affinity matrix \mathbf{W} to determine the output $\{\text{Id}_i\}_{i=1}^N$
-

The following theorem asserts that TGCT achieves correct clustering with high probability. Its proof is in Section 5. Its statement relies on the constants $\{C_i\}_{i=0}^6$ and C'_0 , which are clarified in the proof and depend only on the underlying geometry of the generative model. For simplicity, the theorem assumes that there are only two geodesic submanifolds and that they are of the same dimension. However, it can be extended to K geodesic submanifolds of different dimensions.

Theorem 1 Consider two smooth compact d -dimensional geodesic submanifolds, S_1 and S_2 , of a Riemannian manifold and let X be a dataset generated according to uniform MGM w.r.t. $S_1 \cup S_2$ with noise level τ . If the positive parameters of the TGCT algorithm, r , σ_d , σ_a and η , satisfy the inequalities

$$\begin{aligned} \eta < C_2^{-\frac{d+2}{2}}, \sigma_d < C_4^{-\frac{1}{2}}, r > \tau/C_5, r < \min(\eta, \sigma_d, \sigma_a)/C_1 \quad \text{and} \\ \sigma_a < \min(\sin^{-1}(r\sqrt{1 - C_2\eta^{\frac{2}{d+2}}/(2\sigma_d)}) - C_3\eta^{\frac{d}{d+2}} - C_3r, \pi/6), \end{aligned} \quad (2)$$

then with probability at least $1 - C_0N \exp[-Nr^{d+2}/C'_0]$, the TGCT algorithm can cluster correctly a sufficiently large subset of X , whose relative fraction (over X) has expectation at least $1 - C_6(r + \tau)^{d - \dim(S_1 \cap S_2)}$.

3.2.2 Algorithm 2: Geodesic Clustering with Tangent information (GCT)

A practical version of the TGCT algorithm, which we refer to as Geodesic Clustering with Tangent information (GCT), is described in Algorithm 2. This is the algorithm implemented for the experiments in Section 4 and its choice of parameters is clarified in Section A.2. GCT differs from TGCT in three different ways. First, hard thresholds in TGCT are replaced by soft ones, which are more flexible. Second,

the dimension indicator function is dropped from the affinity matrix W . Indeed, numerical experiments indicate that the algorithm works properly without the dimension indicator function, whenever there is only a small portion of points near the intersection. This numerical observation makes sense since the dimension indicator is only used in theory to avoid connecting intersection points to points not in intersection. At last, pairwise distances are replaced by weights resulting from sparsity-cognizant optimization tasks. Sparse coding takes advantage of the low-dimensional structure of submanifolds and produces larger weights for points coming from the same submanifold (Elhamifar and Vidal, 2011).

Algorithm 2 Geodesic Clustering with Tangent information (GCT)

Input: Number of clusters: $K \geq 2$, a dataset X of N points, a neighborhood radius r , a distance threshold σ_d (default: $\sigma_d = 1$) and an angle threshold σ_a (default $\sigma_a = 1$)

Output: Index set $\{\text{Id}_i\}_{i=1}^N$ such that $\text{Id}_i \in \{1, \dots, K\}$ is the cluster label assigned to x_i

Steps:

for $i = 1, \dots, N$ **do**

- For $j \in J(x_i, r)$, compute $\mathbf{x}_j^{(i)} = \log_{x_i}(x_j)$
- Compute the weights $\{\mathbf{S}_{ij}\}_{j \in J(x_i, r)}$ that minimize

$$\|\mathbf{x}_i^{(i)} - \sum_{\substack{j \in J(x_i, r) \\ j \neq i}} \mathbf{S}_{ij} \mathbf{x}_j^{(i)}\|_2^2 + \sum_{\substack{j \in J(x_i, r) \\ j \neq i}} e^{\|\mathbf{x}_i^{(i)} - \mathbf{x}_j^{(i)}\|_2 / \sigma_d} |\mathbf{S}_{ij}| \quad (3)$$

among all $\{\mathbf{S}_{ij}\}_{j \in J(x_i, r)}$ such that $\mathbf{S}_{ii} = 0$ and $\sum_{\substack{j \in J(x_i, r) \\ j \neq i}} \mathbf{S}_{ij} = 1$

- Complete these weights as follows: $\mathbf{S}_{ij} = 0$ for $j \notin J(x_i, r)$
- Compute the sample covariance matrix \mathbf{C}_{x_i} of $\{\mathbf{x}_j^{(i)}\}_{j \in J(x_i, r)}$
- Find the largest gap between eigenvalues λ_m and λ_{m+1} of \mathbf{C}_{x_i} and compute the top m eigenvectors of \mathbf{C}_{x_i} (their span is $T_{x_i}^E S$)
- For all $j = 1, \dots, N$, compute the empirical geodesic angles θ_{ij} (see Section 3.1)

end for

- Form the following $N \times N$ affinity matrix \mathbf{W} :

$$\mathbf{W}_{ij} = e^{|\mathbf{S}_{ij}| + |\mathbf{S}_{ji}|} e^{-(\theta_{ij} + \theta_{ji}) / \sigma_a} \quad (4)$$

- Apply spectral clustering to the affinity matrix W to determine the output $\{\text{Id}_i\}_{i=1}^N$
-

Algorithm 2 solves a sparse coding task in (3). The penalty used is non-standard since the codes $|\mathbf{S}_{ij}|$ are multiplied by $e^{\|\mathbf{x}_i^{(i)} - \mathbf{x}_j^{(i)}\|_2 / \sigma_d}$ (where in Cetingul et al. (2014), these latter terms are all 1). These weights were chosen to increase the effect of nearby points (in addition to their sparsity). In particular, it avoids sparse representations via far-away points that are unrelated to the local manifold structure (see further explanation in Figure 4). Similarly to Cetingul et al. (2014), the clustering weights in (4) exponentiate the sparse-coding weights.

3.2.3 Computational Complexity of GCT and TGCT

We briefly discuss the computational complexity of GCT and TGCT, while leaving many technical details to Appendices B and C. The computational complexity of GCT is

$$\mathcal{O}(N^2(\text{CR} + \text{CL} + D) + kN \log(N) + ND + Nk^3),$$

where k bounds the number of nearest neighbors in a neighborhood (typically $k = 30$ by the choice of parameters), CR is the cost of computing the Riemannian distances between any two points and CL is the

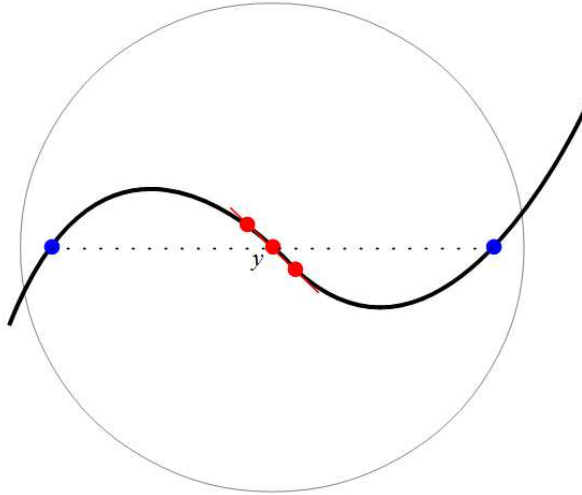


Figure 4: Illustration of the need for weighted sparse optimization in (3). The non-weighted sparse optimization may fail to detect the local structure at y in the manifold setting. The term $e^{\|\mathbf{x}_i^{(i)} - \mathbf{x}_j^{(i)}\|_2 / \sigma_d}$ is used to avoid assigning large weights to the far-away blue points.

cost of computing the logarithm map of a given point w.r.t. another point. Furthermore, once CL was computed, $CR = \mathcal{O}(D)$. The complexity of CL depends on the Riemannian manifold M . If $M = \mathbb{S}^D$, then $CL = \mathcal{O}(D)$. If M is the space of symmetric PD matrices and $\dim(M) = D$, then $CL = \mathcal{O}(D^{1.5})$. If M is the Grassmannian, $\dim(M) = D$ and d is chosen to be of the same order as the dimension of the subspaces in M , then $CL = d(d + D/d)^2$. In all applications of Riemannian multi-manifold modeling we are aware of M is known and it is one of these examples. For more general or unknown M , estimation of the logarithm map is discussed in Mémoli and Sapiro (2005) (this estimation is rather slow).

It is possible to reduce the total computational cost under some assumptions. In particular, in theory, it is possible to implement TGCT (or more precisely an approximate variant of it) for the sphere or the Grassmannian with computational complexity of order

$$\mathcal{O}(N^{1+\rho}CR + (k+1)N \log(N) + kN(CL + D) + Nk^3),$$

where $\rho > 0$ is near zero.

4 Numerical Experiments

To assess performance on both synthetic and real datasets, the GCT algorithm is compared with the following algorithms: Sparse manifold clustering (SMC) (Elhamifar and Vidal, 2011; Cetingul et al., 2014), which is adapted here for clustering within a Riemannian manifold and still referred to as SMC, spectral clustering with Riemannian metric (SCR) of Goh and Vidal (2008), and embedded K -means (EKM). The three methods and choices of parameters for all four methods are reviewed in Appendix A.2.

The ground truth labeling is given in each experiment. To measure the accuracy of each method, the assigned labels are first permuted to have the maximal match with the ground truth labels. The clustering rate is computed for that permuted labels as follows:

$$\text{clustering rate} = \frac{\# \text{ of points whose group labels are the same as ground truth labels}}{\# \text{ of total points}}.$$

4.1 Experiments with Synthetic Datasets

Six datasets were generated. Dataset I and II are from the Grassmannian $G(6, 2)$, datasets III and IV are from 3×3 symmetric positive-definite (PD) matrices, and datasets V and VI are from the sphere \mathbb{S}^2 . Each dataset contains 260 points generated from two “parallel” or intersecting submanifolds (130 points on each) and cropped by white Gaussian noise. The exact constructions are described below.

Datasets I and II The first two datasets are on the Grassmannian $G(6, 2)$. In dataset I, 130 pairs of subspaces are drawn from the following non-intersecting submanifolds:

$$\begin{aligned}\mathbf{x}_1 &= \text{Sp}\{(\cos(\theta), 0, \sin(\theta), 0, 0, 0) + \frac{1}{40}\boldsymbol{\epsilon}_{1 \times 6}, (0, \cos(\theta), 0, \sin(\theta), 0, 0) + \frac{1}{40}\boldsymbol{\epsilon}_{1 \times 6}\}, \\ \mathbf{x}_2 &= \text{Sp}\{(\cos(\phi), 0, \sin(\phi), 0, 0.5, 0) + \frac{1}{40}\boldsymbol{\epsilon}_{1 \times 6}, (0, \cos(\phi), 0, \sin(\phi), 0.5, 0) + \frac{1}{40}\boldsymbol{\epsilon}_{1 \times 6}\},\end{aligned}$$

where θ, ϕ are equidistantly drawn from $[-\pi/3, \pi/3]$ and the noise vector $\boldsymbol{\epsilon}_{1 \times 6}$ comprises i.i.d. normal random variables $\mathcal{N}(0, 1)$.

In dataset II, 130 pairs of subspaces lie around two intersecting submanifolds as follows:

$$\begin{aligned}\mathbf{x}_1 &= \text{Sp}\{(\cos(\theta), 0, \sin(\theta), 0, 0, 0) + \frac{1}{40}\boldsymbol{\epsilon}_{1 \times 6}, (0, \cos(\theta), 0, \sin(\theta), 0, 0) + \frac{1}{40}\boldsymbol{\epsilon}_{1 \times 6}\}, \\ \mathbf{x}_2 &= \text{Sp}\{(\cos(\phi), 0, 0, 0, \sin(\phi), 0) + \frac{1}{40}\boldsymbol{\epsilon}_{1 \times 6}, (0, \cos(\phi), 0, 0, 0, \sin(\phi)) + \frac{1}{40}\boldsymbol{\epsilon}_{1 \times 6}\},\end{aligned}$$

where θ, ϕ are equidistantly drawn from $[-\pi/3, \pi/3]$ and the noise vector $\boldsymbol{\epsilon}_{1 \times 6}$ comprises, again, i.i.d. normal random variables $\mathcal{N}(0, 1)$.

Datasets III and IV The next two datasets are contained in the manifold of 3×3 symmetric PD matrices.

In dataset III, 130 pairs of matrices of two intersecting groups are generated from the model

$$\begin{aligned}\mathbf{A}_1 &= \begin{pmatrix} 4 & 4 \cos(\theta + \pi/4) & 4 \sin(\theta + \pi/4) \\ 4 \cos(\theta + \pi/4) & 4 & 0 \\ 4 \sin(\theta + \pi/4) & 0 & 4 \end{pmatrix} + \boldsymbol{\epsilon}_{3 \times 3}/40, \\ \mathbf{A}_2 &= \begin{pmatrix} 4 & 0 & 4 \cos(\theta - \pi/4) \\ 0 & 4 & 4 \sin(\theta - \pi/4) \\ 4 \cos(\theta - \pi/4) & 4 \sin(\theta + \pi/4) & 4 \end{pmatrix} + \boldsymbol{\epsilon}_{3 \times 3}/40,\end{aligned}\tag{5}$$

where θ is equidistantly drawn from $[0, \pi]$ and $\boldsymbol{\epsilon}_{3 \times 3}$ is a symmetric matrix whose entries are i.i.d. normal random variables with distribution $\mathcal{N}(0, 1)$.

In dataset IV, 130 pairs of matrices of two non-intersecting groups are generated from the model

$$\mathbf{A}_1 = \begin{pmatrix} 10\alpha & 0 & 0 \\ 0 & 10\alpha & 0 \\ 0 & 0 & 10\alpha \end{pmatrix} + \boldsymbol{\epsilon}_{3 \times 3}/40, \quad \mathbf{A}_2 = \begin{pmatrix} 10\beta & 0 & 0 \\ 0 & 10\beta^2 & 0 \\ 0 & 0 & 10\beta^3 \end{pmatrix} + \boldsymbol{\epsilon}_{3 \times 3}/40,$$

where α, β are equidistantly drawn from $[0.5, 1]$ respectively and $\boldsymbol{\epsilon}_{3 \times 3}$ is a symmetric matrix whose entries are i.i.d. normal random variables with distribution $\mathcal{N}(0, 1)$.

Methods	Set I	Set II	Set III	Set IV	Set V	Set VI
GCT	1.00 ±0.00	0.98 ±0.01	0.98 ±0.00	0.95 ±0.01	0.98 ±0.01	0.96 ±0.01
SMC	0.97 ±0.04	0.66 ±0.08	0.88 ±0.03	0.80 ±0.02	0.55 ±0.06	0.69 ±0.05
SCR	0.51 ±0.00	0.66 ±0.07	0.84 ±0.00	0.80 ±0.00	0.50 ±0.00	0.53 ±0.07
EKM	0.50 ±0.00	0.50 ±0.00	0.67 ±0.00	0.50 ±0.00	0.50 ±0.00	0.67 ±0.06

Table 1: Average clustering rates on the six synthetic datasets of Section 4.1.

Datasets V and VI Two datasets are constructed on the unit sphere \mathbb{S}^2 of the 3-dimensional Euclidean space. Dataset V comprises of vectors lying around the following two parallel arcs:

$$\begin{aligned}\mathbf{x}_1 &= [\cos(\theta), \sin(\theta), 0] + \boldsymbol{\epsilon}_{1 \times 3}, \\ \mathbf{x}_2 &= [\sqrt{0.97} \cos(\phi), \sqrt{0.97} \sin(\phi), \sqrt{0.03}] + \boldsymbol{\epsilon}_{1 \times 3},\end{aligned}$$

where θ, ϕ are equidistantly drawn from $[0, \pi/2]$. To ensure membership in \mathbb{S}^2 , vectors generated by \mathbf{T}_1 and \mathbf{T}_2 are normalized to unit length. On the other hand, dataset VI considers the following two intersecting arcs:

$$\begin{aligned}\mathbf{x}_1 &= [\cos(\theta + \pi/4), \sin(\theta + \pi/4), 0] + \frac{1}{40} \boldsymbol{\epsilon}_{1 \times 3}, \\ \mathbf{x}_2 &= [0, \cos(\phi - \pi/4), \sin(\phi - \pi/4)] + \frac{1}{40} \boldsymbol{\epsilon}_{1 \times 3}.\end{aligned}$$

4.1.1 Numerical Results

Each one of the six datasets is generated according to the postulated models above, and the experiment is repeated 30 times. Table 1 shows the average clustering rate for each method. GCT, SMC and SCR are all based on the spectral clustering scheme. However, when a dataset has low-dimensional structures, GCT’s unique procedure of filtering neighboring points ensures that it yields superior performance over the other methods. This is because both SMC and SCR are sensitive to the local scale σ , and require each neighborhood not to contain points from different groups. This becomes clear by the results on datasets I, IV, and V of non-intersecting submanifolds. SMC only works well in dataset I, where most of the neighborhoods $B(x_0, r)$ contain only points from the same cluster, while neighborhoods $B(x_0, r)$ in datasets IV and V often contain points from different ones. Embedded K -means generally requires that the intrinsic means of different clusters are located far from each other. Its performance is not as good as GCT when different groups have low-dimensional structures.

4.2 Robustness to Noise and Running Time

Section 4.1 illustrated GCT’s superior performance over the competing SMC, SCR, and EKM on a variety of manifolds. This section further investigates GCT’s robustness to noise and computational cost pertaining to running time. In summary, GCT is shown to be far more robust than SMC in the presence of noise, at the price of a small increase of running time.

4.2.1 Robustness to Noise

The proposed tangent filtering scheme enables GCT to successfully eliminate neighboring points that originate from different groups. As such, it exhibits robustness in the presence of noise and/or whenever different groups are close or even intersecting. On the other hand, SMC appears to be sensitive to noise

due to its sole dependence on sparse weights. Figures 5 and 6 demonstrate the performance of GCT, SMC, SCR, and EKM on the Grassmannian and the sphere for various noise levels (standard deviations of Gaussian noise).

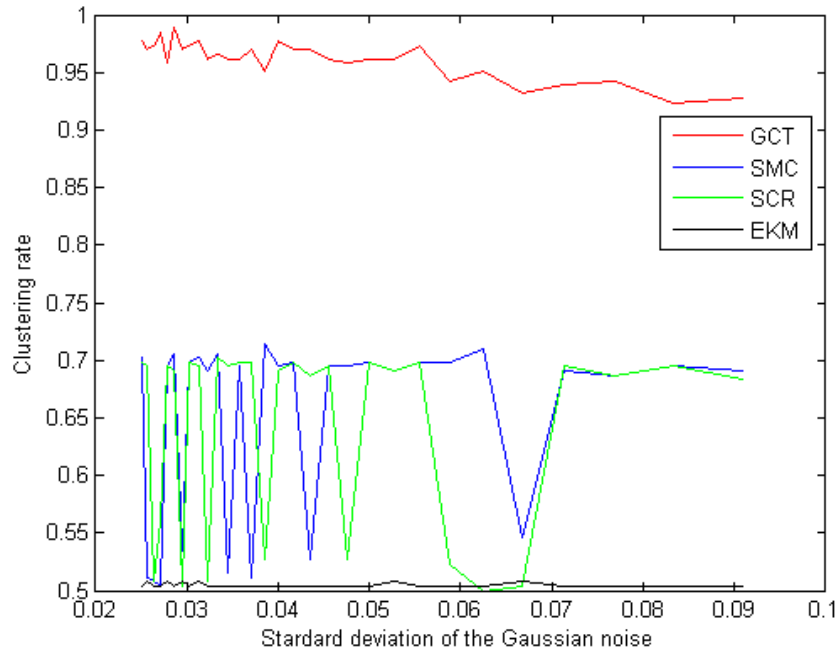


Figure 5: Performance of clustering methods on the Grassmannian for various noise levels. Datasets are generated according to the model of dataset II, but with an increasing standard deviation of the noise.

The datasets in Figure 5 are generated on the Grassmannian according to the model of dataset II in Section 4.1 but with different noise levels (in Section 4.1 the noise level was 0.025). Both SMC and SCR appear to be volatile over different datasets, with their best performance never exceeding 0.75 clustering rate. It is worth noticing that EKM shows poor clustering accuracy. On the contrary, GCT exhibits remarkable robustness to noise, achieving clustering rates above 0.9 even when the standard deviation of the noise approaches 0.1.

GCT’s robustness to noise is also demonstrated in Figure 6, where datasets are generated on the unit sphere according to the model of the dataset VI, but with different noise levels. SMC appears to be volatile also in this setting; it collapses when the standard deviation of noise exceeds 0.05, since its affinity matrix precludes spectral clustering from identifying eigenvalues with sufficient accuracy (see further explanation on the collapse of SMC at the end of Section A.2).

4.2.2 Running time

This section demonstrates that GCT outperforms SMC at the price of a small increase in computational complexity. Similarly to any other manifold clustering algorithm, computations have to be performed per local neighborhood, where local linear structures are leveraged to increase clustering accuracy. The overall complexity scales quadratically w.r.t. the number of data-points due to the last step of Algorithm 2, which amounts to spectral clustering of the $N \times N$ affinity matrix \mathbf{W} . Both the optimization task of (3) and the computation of a few principal eigenvectors of the covariance matrix \mathbf{C}_{x_i} in Algorithm 2 do not contribute much to the complexity since operations are performed on a small number of points in the neighborhood $J(x_i, r)$. The computational complexity of GCT is detailed in Appendix C. It is also noteworthy that GCT

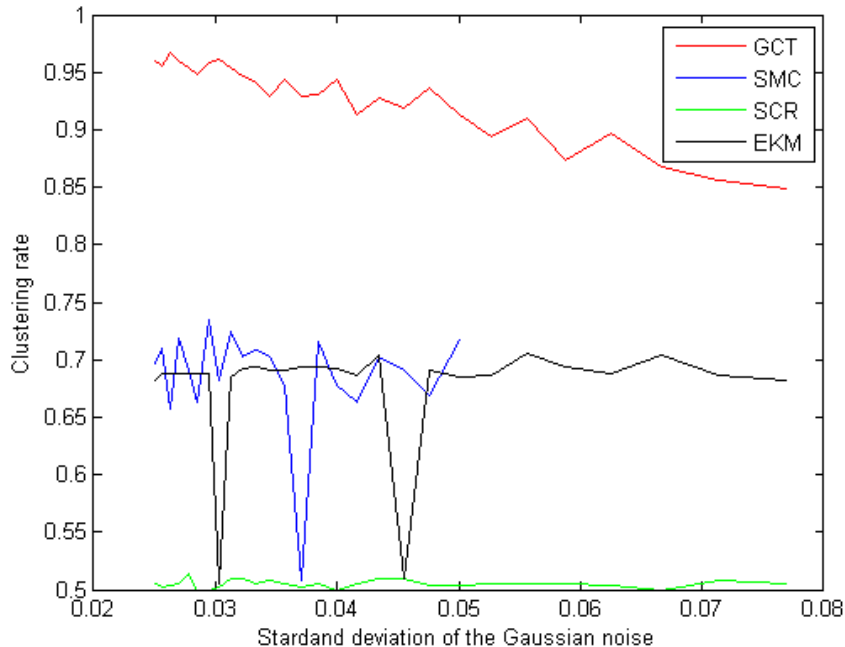


Figure 6: Performance of clustering methods on the sphere for various noise levels. Datasets are generated according to the model of dataset VI, but with an increasing standard deviation of the noise.

Running-time ratio	$G(6, 2)$	$PD_{3 \times 3}$	S^2
GCT/SMC	1.06	1.05	1.11

Table 2: Ratio of running times of GCT and SMC for instances of the synthetic datasets I, IV and VI

can be fully parallelized since computations per neighborhood are independent. Nevertheless, such a route is not followed in this section.

Compared with SMC, GCT has one additional component: identifying tangent spaces through local covariance matrices—a task that entails local calculation of a few principal eigenvectors. Nevertheless, it is shown in Appendix C.1 that for k neighbors it can be calculated with $\mathcal{O}(D + k^3)$ operations.

The ratios of running times between GCT and SMC for all three types of manifolds are illustrated in Table 2. It can be readily verified that the extra step of identifying tangent spaces in GCT increases running time by less than 11% of the one for SMC.

Ratios of running times were also investigated for increasing ambient dimensions of the sphere. More precisely, dataset VI of Section 4.1, which lies in S^2 , was embedded via a random orthonormal matrix into the unit sphere S^D , where D ranged from 100 to 3,000. Figure 7 shows the ratios of the running time of GCT over that of SMC as a function of D . We observe that the extra cost of computing the eigendecomposition in GCT is mostly less than 20% of SMC, and never exceeds 30%, even when the ambient dimension is as large as 3,000.

4.3 Synthetic Brain Fibers Segmentation

Cetingul et al. (2014) cast the problem of segmenting diffusion magnetic resonance imaging (DMRI) data of different fiber tracts as a clustering problem on S^D . The crux of the methodology lies on the transfor-

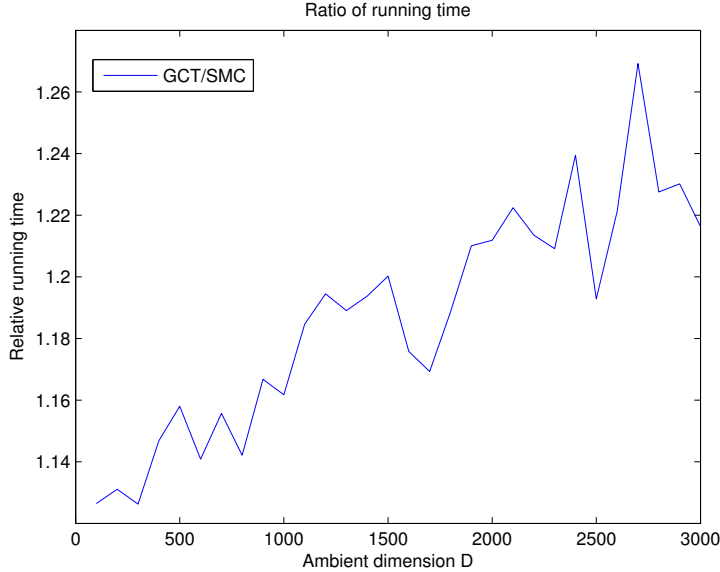


Figure 7: Relative running times of GCT w.r.t. SMC as the ambient dimension increases. With dimensions D ranging from 100 to 3,000, dataset VI of Section 4.1 was embedded via a random orthonormal matrix into the unit sphere \mathbb{S}^D . Dataset VI of Section 4.1 matrix with two random

mation of diffusion images, associated with different views of the same object, into orientation distribution functions (ODFs), which are nothing but probability density functions on \mathbb{S}^2 . The discretized ODF (dODF) is a probability mass function (pmf) $\mathbf{f} : (\mathbb{S}^2)^{D+1} \rightarrow \mathbb{R}_+^{D+1} : (\mathbf{s}_1, \dots, \mathbf{s}_{D+1}) \mapsto \mathbf{f}(\mathbf{s}_1, \dots, \mathbf{s}_{D+1}) := [f_1(\mathbf{s}_1), \dots, f_{D+1}(\mathbf{s}_{D+1})]^T$, with $\sum_{i=1}^{D+1} f_i(\mathbf{s}_i) = 1$, that describes the water diffusion pattern at a corresponding location of the object’s image according to the viewing directions $\{\mathbf{s}_i\}_{i=1}^{D+1}$. Given $\{\mathbf{s}_i\}_{i=1}^{D+1}$ and a fixed location, the *square-root* (SR)dODF is the vector $\sqrt{\mathbf{f}}(\mathbf{s}_1, \dots, \mathbf{s}_{D+1}) := [\sqrt{f_1(\mathbf{s}_1)}, \dots, \sqrt{f_{D+1}(\mathbf{s}_{D+1})}]^T$, which lies on the sphere \mathbb{S}^D since \mathbf{f} is a pmf. In this way, pixels of diffusion images of the same object at a given location are mapped into an element of \mathbb{S}^D . Cetingul et al. (2014) assume that each fiber tract is mapped into a submanifold of \mathbb{S}^D and thus try to identify different fiber tracts by multi-manifold modeling on \mathbb{S}^D .

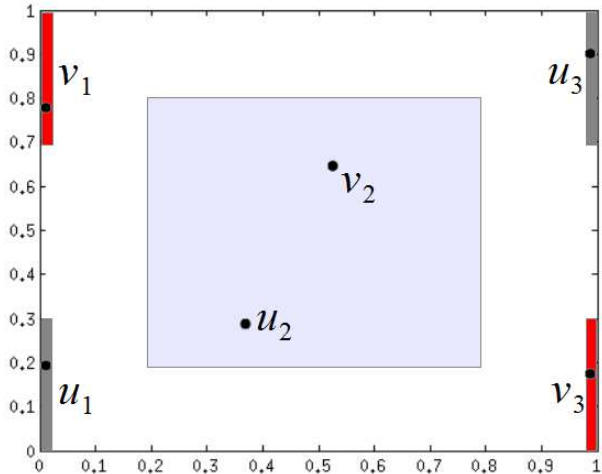
As suggested in Cetingul et al. (2014), to differentiate pixels with similar diffusion patterns but located far from each other in an image, one has to incorporate pixel spatial information in the segmentation algorithm. Therefore, for GCT, SMC and SCR, the similarity entry \mathbf{W}_{ij} of two pixels $\mathbf{x}_i, \mathbf{x}_j \in \mathbb{R}^2$ is modified as

$$\mathbf{W}_{ij}^{\text{new}} = \mathbf{W}_{ij} \cdot e^{-\|\mathbf{x}_i - \mathbf{x}_j\|_2^2 / \sigma},$$

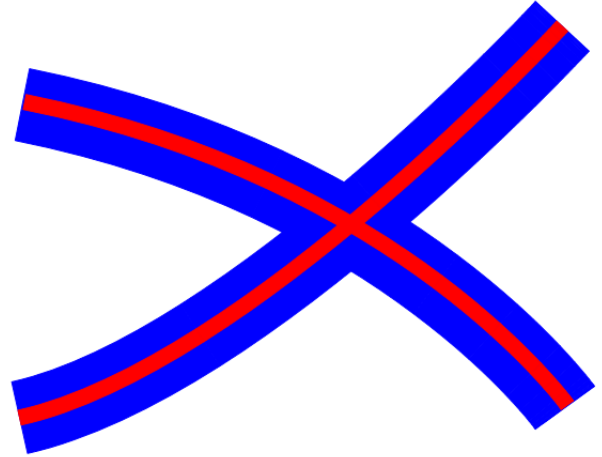
where \mathbf{W} is the similarity matrix before modification (e.g., for GCT, it is described in Algorithm 2), $\sigma = 0.1$ and $\|\mathbf{x}_i - \mathbf{x}_j\|_2$ is the Euclidean distance between two pixels. For EKM, where no spectral clustering is employed, the dODF is simply augmented with the spatial coordinates of \mathbf{x}_i and \mathbf{x}_j .

Following Cetingul et al. (2014), we consider here the problem of segmenting or clustering two 2D synthetic fiber tracts in the $[0, 1] \times [0, 1]$ domain. To generate the fibers, six points $\mathbf{u}_1, \mathbf{u}_2, \mathbf{u}_3, \mathbf{v}_1, \mathbf{v}_2, \mathbf{v}_3$ are randomly chosen in the colored region of Figure 8a. Two cubic splines passing through $\{\mathbf{u}_1, \mathbf{u}_2, \mathbf{u}_3\}$ and $\{\mathbf{v}_1, \mathbf{v}_2, \mathbf{v}_3\}$, respectively, are set to be the center of the fibers (cf., red curves in Figure 8b). Fibers are defined as the curved bands around the splines with bandwidth 0.12 (cf., blue region in Figure 8b).

Given a pair of such fibers, the next step is to map each pixel (e.g., both red and blue ones in Figure 8b) to a point (SRdODF) in \mathbb{S}^D . To this end, the software code provided by Canales-Rodriguez et al. (2013) is used to generate SRdODFs on \mathbb{S}^{100} , where diffusion images $\{S_n\}_{n=1}^G$ at $G = 70$ gradient directions,



(a) Randomly sampled 6 points from the colored regions of the $[0, 1] \times [0, 1]$ domain.



(b) A configuration of two intersecting fibers generated according to points in Figure 8a

Figure 8: Demonstration of fiber generation. Two fibers are generated in Figure 8b by fitting two cubic splines to $\{\mathbf{u}_i\}_{i=1}^3$ and $\{\mathbf{v}_i\}_{i=1}^3$ in Figure 8a, respectively.

Methods	SNR=40	SNR=30	SNR=20	SNR=10
GCT	0.80 ± 0.12	0.82 ± 0.12	0.78 ± 0.14	0.80 ± 0.13
SMC	0.73 ± 0.14	0.73 ± 0.13	0.70 ± 0.13	0.67 ± 0.13
SCR	0.66 ± 0.11	0.66 ± 0.11	0.68 ± 0.11	0.66 ± 0.11
EKM	0.59 ± 0.08	0.58 ± 0.08	0.61 ± 0.08	0.59 ± 0.08

Table 3: Mean \pm standard deviation of accuracy rates for 100 experiments on clustering synthetic brain fibers.

with baseline image $S_0 = 100$ and $b = 4,000\text{s}/\text{mm}^2$, are considered. The dimensionality of the generated SRdODFs corresponds to 100 directions. Moreover, Gaussian noise $\mathcal{N}(0, \sigma^2)$ was added in the ODF-generation mechanism, resulting in a signal-to-noise ratio $\text{SNR} = S_0/\sigma$ (more details on the construction can be found in Cetingul et al. (2014)). Typical noise levels for real-data brain images are considered: $\text{SNR} = 10, 20, 30$, and 40 (i.e., $\sigma = 10, 5, 10/3, 2.5$).

Once SRdODFs are formed, clustering is carried out on the Riemannian manifold \mathbb{S}^D . This in turn provides a segmentation of pixels according to different fiber tracts. A total number of 100 pairs of synthetic brain fibers are randomly generated, and clustering is performed for each pair. Table 3 reports the mean \pm standard deviation of the clustering accuracy rates. Results clearly suggest that GCT outperforms the other three clustering methods. For the case of $\text{SNR} = 10$, Figure 9 plots sample distributions of accuracy rates and shows that GCT demonstrates the highest probability of achieving almost accurate clustering among competing schemes.

4.4 Experiments with Real Data

In this section, GCT performance is assessed on real datasets. Scenarios where data within each cluster have submanifold structures are demonstrated.

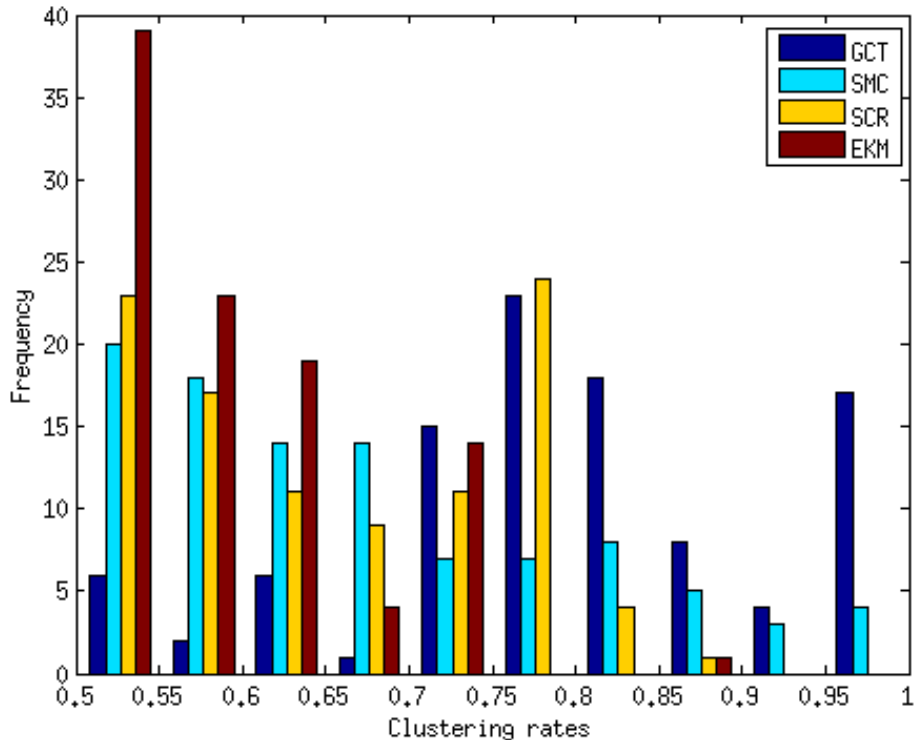


Figure 9: Histogram of clustering rates for the noise level $\text{SNR} = 10$ over a total number of 100 experiments. Each bar shows the number of experiments whose rates fall within one of the ten intervals of length 0.05 in the partition. For example, since the tallest bar within the $[0.95, 1]$ range is the blue one, GCT is the most likely method to achieve almost accurate clustering. On the contrary, the brown bar is the tallest one between the range of 0.5 and 0.55, meaning that a clustering rate within $[0.5, 0.55]$ is the most likely one to be achieved for EKM over 100 experiments.

4.4.1 Stylized Application: Texture Clustering

We cluster local covariance matrices obtained from various transformations of images of the Brodatz database (Randen, 2014) where the goal is to be able to distinguish between the different images independently of the transformation.

The Brodatz database contains 112 images of 640×640 pixels with different textures (e.g., brick wall, beach sand, grass) captured under uniform lighting and in frontview position. We apply three simple deformations to these images, which mimic real settings: different lighting conditions, stretching (obtained by shearing) and different viewpoints (obtained by affine transformation). Figure 10 shows sample images in the Brodatz database and their deformations.

Tou et al. (2009) show that region covariances generated by Gabor filters effectively represent texture patterns in a region (patch). Given a patch of size 60×60 , a Gabor filter of size 11×11 with 8 parameters is used to extract 2,500 feature vectors of length 8. This set of feature vectors is then used to compute an 8×8 covariance matrix for the specific patch.

Three clustering tests, one for each type of deformation, are carried out. In each test, 300 transformed patches are generated equally from 3 different textures and the region covariance is computed for each patch. Then clustering algorithms are applied on the dataset of 300 region covariances belonging to 3 texture patterns. The way to generate transformed patches is described below.

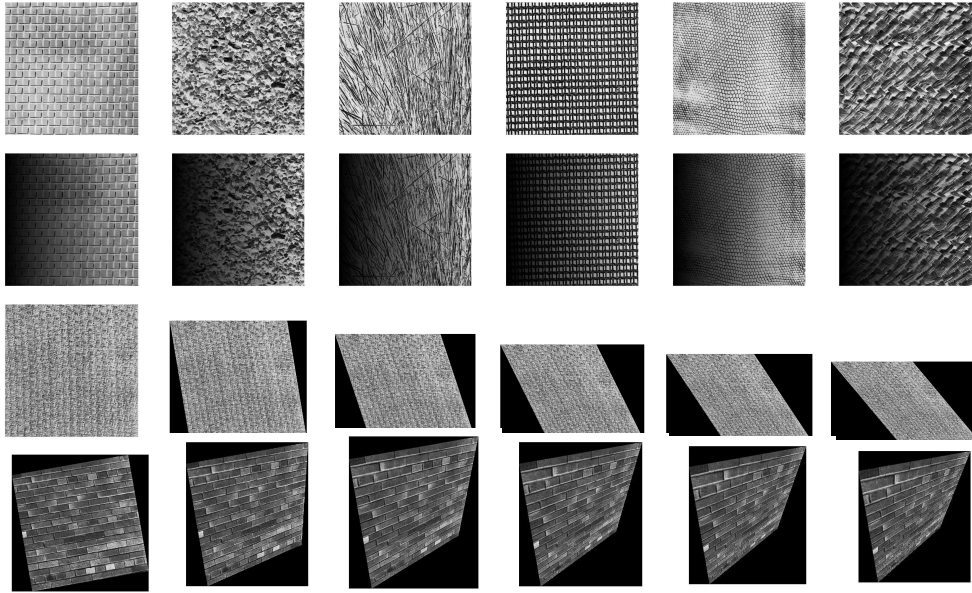


Figure 10: Sample images in the Brodatz database and their deformations. The first row shows the 6 original images; in the second row, each image contains a unique texture but different regions of it have different lighting; the third row shows the horizontal-shifted (distorted) images of an image; the fourth row shows affine-transformed (change of viewpoints) images of an image.

	Methods	GCT	SMC	SCR	EKM
Lighting transformation		0.73	0.53	0.68	0.67
Horizontal shifting		0.95	0.61	0.85	0.76
Affine transformation		0.83	0.53	0.82	0.76

Table 4: Average clustering rates for each method over 30 datasets.

I. Lighting transformation: A single lighting transformation (demonstrated in Figure 10) is applied to three randomly drawn images from the Brodatz database and 100 patches of size 60×60 are randomly picked from each of the 3 transformed images.

II. Horizontal shearing: Three randomly drawn images are horizontally sheared by 100 different angles to get 3 sequences of 100 shifted images. From each shifted image, a patch of size 60×60 is randomly picked.

III. Affine transformation: Three randomly drawn images are affine transformed to create 3 sequences of 100 affine-transformed images. From each transformed image, a patch of size 60×60 is randomly picked.

Figure 11 plots the projection of the embedded datasets generated by the above procedure onto their top three principal components (the embedding to Euclidean spaces is done by direct vectorization of the covariance matrices). The submanifold structure in each cluster can be easily observed.

The procedure of generating the data is repeated 30 times for each type of transformation. GCT as well as the other three clustering methods are applied to these datasets, and the average clustering rates are reported in Table 4. GCT exhibits the best performance for all datasets and for all types of transforms.

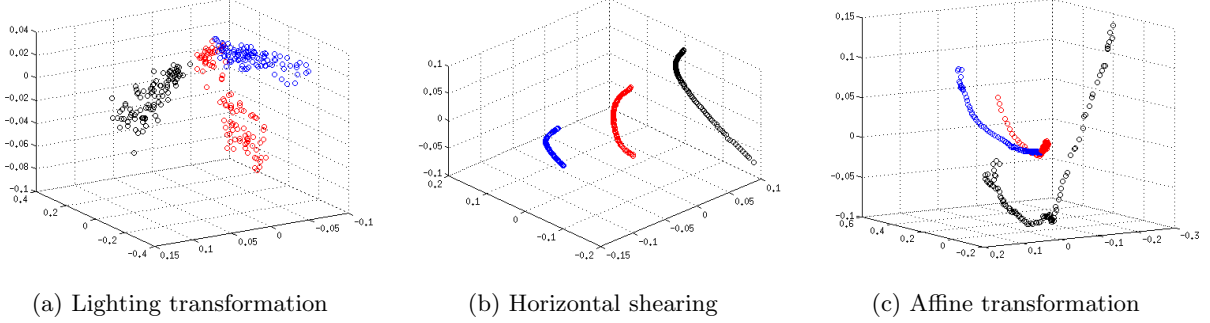


Figure 11: Projection of the covariance matrices of local patches of the transformed 3 images onto their top 3 principal directions. For 3 sample images, a dataset of 300 covariance matrices is computed for each transformation type. The 8×8 covariance matrices are identified as vectors in \mathbb{R}^{64} . The figure demonstrates the underlying structure of 3 manifolds for the data generated with each kind of transformation.

4.4.2 Clustering Dynamic Patterns.

Spatio-temporal data such as dynamic textures and videos of human actions can often be approximated by linear dynamical models (Doretto et al., 2003; Turaga et al., 2011). In particular, by leveraging the autoregressive and moving average (ARMA) model, we experiment here with two spatio-temporal databases: Dyntex++ and Ballet. Following Turaga et al. (2011), we employ the ARMA model to associate local spatio-temporal patches with linear subspaces of the same dimension. We then apply manifold clustering on the Grassmannian in order to distinguish between different textures and actions in the Dyntex++ and Ballet database respectively.

ARMA Model. The premise of ARMA modeling is based on the assumption that the spatio-temporal dataset under study is governed by a small number of latent variables whose temporal variations obey a linear rule. More specifically, if $\mathbf{f}(t) \in \mathbb{R}^p$ is the observation vector at time t (in our case, it is the vectorized image frame of a video sequence), then

$$\begin{aligned} \mathbf{f}(t) &= \mathbf{C}\mathbf{z}(t) + \boldsymbol{\epsilon}_1(t) & \boldsymbol{\epsilon}_1(t) &\sim N(\mathbf{0}, \boldsymbol{\Sigma}_1) \\ \mathbf{z}(t+1) &= \mathbf{A}\mathbf{z}(t) + \boldsymbol{\epsilon}_2(t) & \boldsymbol{\epsilon}_2(t) &\sim N(\mathbf{0}, \boldsymbol{\Sigma}_2) \end{aligned} \quad (6)$$

where $\mathbf{z}(t) \in \mathbb{R}^d$, $d \leq p$, is the vector of latent variables, $\mathbf{C} \in \mathbb{R}^{p \times d}$ is the observation matrix, $\mathbf{A} \in \mathbb{R}^{d \times d}$ is the transition matrix, and $\boldsymbol{\epsilon}_1(t) \in \mathbb{R}^p$ and $\boldsymbol{\epsilon}_2(t) \in \mathbb{R}^d$ are i.i.d. sampled vector-values r.v.s. obeying the Gaussian distributions $\mathcal{N}(\mathbf{0}, \boldsymbol{\Sigma}_1)$ and $\mathcal{N}(\mathbf{0}, \boldsymbol{\Sigma}_2)$, respectively.

We next explain the idea of Turaga et al. (2011) to associate subspaces with spatio-temporal data. Given data $\{\mathbf{f}(t)\}_{t=\tau_1}^{\tau_2}$, the ARMA parameters \mathbf{A} and \mathbf{C} can be estimated according to the procedure in Turaga et al. (2011). Moreover, by arbitrarily choosing $\mathbf{z}(0)$, it can be verified that for any $m \in \mathbb{N}$,

$$\mathbb{E} \begin{bmatrix} \mathbf{f}(\tau_1) \\ \mathbf{f}(\tau_1 + 1) \\ \vdots \\ \mathbf{f}(\tau_1 + m - 1) \end{bmatrix} = \begin{bmatrix} \mathbf{C} \\ \mathbf{C}\mathbf{A} \\ \vdots \\ \mathbf{C}\mathbf{A}^{m-1} \end{bmatrix} \mathbf{z}(\tau_1).$$

We then set $\mathbf{V} := [\mathbf{C}^T, (\mathbf{C}\mathbf{A})^T, \dots, (\mathbf{C}\mathbf{A}^{m-1})^T]^T \in \mathbb{R}^{mp \times d}$, which is known as the m th order observability matrix. If the observability matrix is of full column rank, which was the case in all of the conducted

experiments, the column space of \mathbf{V} is a d -dimensional linear subspace of \mathbb{R}^{pm} . In other words, the ARMA model estimated from data $\{\mathbf{f}(t)\}_{t=\tau_1}^{\tau_2}$, $\tau_1 \leq \tau_2$, gives rise to a point on the Grassmannian $G(mp, \ell)$. For a fixed dataset $\{\mathbf{f}(t)\}_{t=1}^{\tau}$, different choices of (τ_1, τ_2) , s.t. $\tau_1, \tau_2 \leq \tau$, and several local regions within the image give rise to different estimates of \mathbf{A} and \mathbf{C} and thus to different points in $G(mp, \ell)$.

Dynamic textures. The Dyntex++ database (Ghanem and Ahuja, 2010) contains 3600 dynamic textures videos of size $50 \times 50 \times 50$, which are divided into 36 categories. It is a hard-to-cluster database due to its low resolution. Three videos were randomly chosen, each one from a distinct category from the available 36 ones.

Per video sequence, 50 patches of size $40 \times 40 \times 20$ are randomly chosen. Each frame of the patch is vectorized resulting into patches of size 1600×20 . To reduce the size to 30×20 , a (Gaussian) random (linear) projection operator is applied to each patch. As a result, each patch is reduced to the set $\{\mathbf{f}(t)\}_{t=\tau_1}^{\tau_1+20} \subset \mathbb{R}^{30}$. We fix $d = 3$ and $m = 3$ and use each such set $\{\mathbf{f}(t)\}_{t=\tau_1}^{\tau_1+20}$ to estimate the underlying ARMA model. Consequently, 150 points on $G(90, 3)$ are generated, 50 per video category.

We expect that points in $G(90, 3)$ of the same cluster lie near a submanifold of $G(90, 3)$. This is due to the repeated pattern of textures in space and time (they often look like a shifted version of each other in space and time). To visualize the submanifold structure, we isometrically embedded $G(90, 3)$ into a Euclidean space (Basri et al., 2011), so that subspaces are mapped to Euclidean points. We then projected the latter points on their top 3 principal components. Figure 13a demonstrates this projection as well as the submanifold structure within each cluster.

Ballet database. The Ballet database (Wang and Mori, 2009) contains 44 videos of 8 actions from a ballet instruction DVD. The frames of all videos are of size 301×301 and their lengths vary and are larger than 100. Different performers have different attire and speed. Three videos, each one associated with a different action, were randomly chosen.



Figure 12: Two samples of Ballet video sequences: the first and second rows are from videos demonstrating actions of hopping and leg-swinging, respectively.

Spatio-temporal patches are generated by selecting 10 consecutive frames of size 301×301 from each one of the following overlapping time intervals: $\{1, \dots, 10\}$, $\{4, \dots, 13\}$, $\{7, \dots, 16\}$, \dots , $\{91, \dots, 100\}$. In this way, for each of the three videos, 31 spatio-temporal patches of size $301 \times 301 \times 10$ are generated. As in the case of the Dyntex++ database, video patches are vectorized and downsized to spatio-temporal patches of size 30×10 . Following the previous ARMA modeling approach, we set $d = 3$ and $m = 3$ and associate each such patch with a subspace in $G(90, 3)$. Consequently, 93 subspaces (31 per cluster) in the Grassmannian $G(90, 3)$ are generated. Figure 13b visualizes the 3D representation of the subspaces created from three random videos. Their intersection represents still motion.

The procedure described above (for generating data by randomly choosing 3 videos from the Dyntex++ and Ballet databases and applying clustering methods on $G(90, 3)$) is repeated 30 times. The average clustering accuracy rates are reported in Table 5. GCT achieves the highest rates on both datasets.

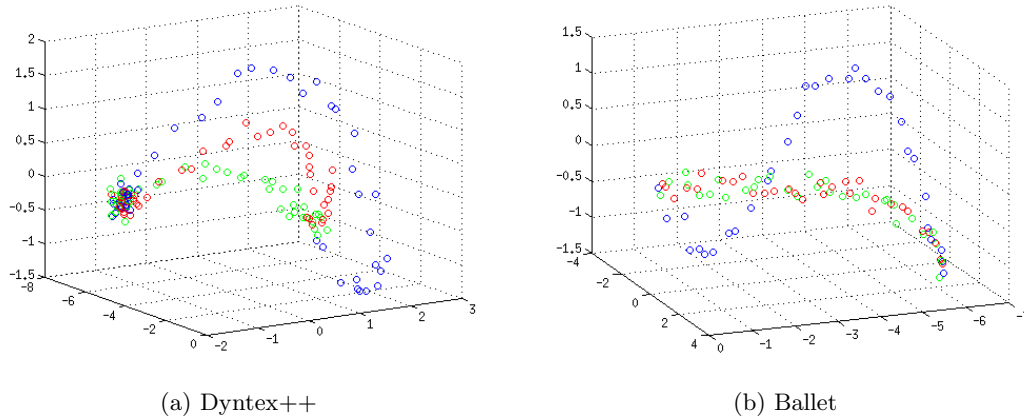


Figure 13: Projection onto top 3 principal components of the two embedded datasets (the embedding into Euclidean spaces is according to Basri et al. (2011)). A submanifold structure for each cluster is clearly depicted.

Methods	GCT	SMC	SCR	EKM
Dyntex++	0.85	0.69	0.77	0.42
Ballet	0.81	0.76	0.68	0.47

Table 5: Average clustering accuracy rates for the Dyntex++ and Ballet datasets.

5 Proof of Theorem 1

The idea of the proof is as follows. After excluding points sampled near the possibly nonempty intersection of submanifolds, we form a graph whose vertices are the points of the remaining set and whose edges are determined by \mathbf{W} . The proof then establishes that the resulting graph has two connected components, which correspond to the two different submanifolds S_1 and S_2 . Spectral clustering can exactly cluster such a graph with appropriate choice of its tuning parameter σ , which can be specified by self-tuning mechanism (Zelnik-Manor and Perona, 2004). This claim follows from Ng et al. (2001) and its unpublished supplemental material.

The basic strategy of the proof and its organization are described as follows. Section 5.1 presents additional notation used in the proof. Section 5.2 reminds the reader the underlying model of the proof (with some additional details). Section 5.3 eliminates undesirable events of negligible probability (it clarifies the term $1 - C_0 N \exp[-Nr^{d+2}/C'_0]$ in the statement of the theorem).

The rest of the proof (described in Sections 5.4-5.8) is briefly sketched as follows. For simplicity, we first assume no noise, i.e., $\tau = 0$. We define a “sufficiently large” set X^* (and its subsets X_1^* and X_2^*) by the following formula (which uses the notation $X_1 = S_1 \cap X$ and $X_2 = S_2 \cap X$):

$$X_1^* = \{x \in X_1 | B(x, r) \cap X_2 = \emptyset\}, X_2^* = \{x \in X_2 | B(x, r) \cap X_1 = \emptyset\} \text{ and } X^* = X_1^* \cup X_2^*. \quad (7)$$

In the first part of the proof (see Section 5.4), we show that the graphs of X_1^* and X_2^* (with weights \mathbf{W}) are respectively connected. If we can show that the graphs of X_1^* and X_2^* are disconnected from each other, then the proof can be concluded. To this end, the subsequent auxiliary sets \hat{X}_1 and \hat{X}_2 will be instrumental in the proof. We fix a constant δ (to be specified later in (34)), which depends on r , η and

the angles of intersection of S_1 and S_2 , and define

$$\hat{X}_1 = \{x \in X_1 \mid \text{dist}_g(x, S_2) \geq \delta\}, \hat{X}_2 = \{x \in X_2 \mid \text{dist}_g(x, S_1) \geq \delta\} \text{ and } \hat{X} = \hat{X}_1 \cup \hat{X}_2. \quad (8)$$

We will verify that $X_1^* \subset \hat{X}_1$ and $X_2^* \subset \hat{X}_2$. In fact, it will be a consequence of the second part of the proof. This part shows that the graph of \hat{X}^c is disconnected from the graph of X_1^* as well as graph of X_2^* . Therefore, X_1^* and X_2^* cannot be connected via points in \hat{X}^c . At last, we show that they also cannot be connected within \hat{X} . That is, we show in the third part of the proof (Section 5.6) that the graphs of \hat{X}_1 and \hat{X}_2 are disconnected from each other. These three parts imply that the graphs of X_1^* and X_2^* form two connected components within X^* . By definition, X_1^* and X_2^* are identified with S_1 and S_2 respectively. To conclude the proof (for the noiseless case), we estimate the measure of the set X^{*c} , which was excluded. More precisely, we consider the measure of the set $X_{S_1 \cap S_2} \supset X^{*c}$, which we define as follows

$$X_{S_1 \cap S_2} = \{x \in X_1 \mid \text{dist}_g(x, S_2) < r\} \cup \{x \in X_2 \mid \text{dist}_g(x, S_1) < r\}. \quad (9)$$

This measure estimate and the conclusion of the proof (to the noiseless case) are established in Section 5.7. Section 5.8 discusses the generalization of the proof to the noisy case.

Various ideas of the proof follow Arias-Castro et al. (2013), which considered multi-manifold modeling in Euclidean spaces. Some of the arguments in the proof of Arias-Castro et al. (2013) even apply to general metric spaces, in particular, to Riemannian manifolds. We thus tried to maintain the notation of Arias-Castro et al. (2013).

However, the algorithm construction and the main theoretical analysis of Arias-Castro et al. (2013) are valid only when the dataset X lies in a Euclidean space and it is nontrivial to extend them to a Riemannian manifold. Indeed, the basic idea of Arias-Castro et al. (2013) is to compare local covariance matrices and use this comparison to infer the relation between the corresponding data points, over which those matrices were generated. However, comparing local covariance matrices in the case where the ambient space is a Riemannian manifold is not straightforward as in Euclidean spaces. This is due to the fact that local covariance matrices are computed at different tangent spaces with different coordinate systems. Instead we show that it is sufficient to compare the ‘‘local directional information’’ (i.e., empirical geodesic angles) and ‘‘local dimension’’. Both of these quantities are derived from the local covariance matrices. However, due to the nonlinear mapping to the tangent spaces, which distorts the uniform assumption within the ambient space, care must be taken in using the inverse nonlinear map, i.e., the logarithm map.

5.1 Notation

We provide additional notation to the one in Section 2.2. Readers are referred to do Carmo (1992) for a complete introduction to Riemannian geometry.

Let $B(x, r)$ and $B_x(\mathbf{0}, r)$ denote the r -neighborhoods of x and $\mathbf{0}$ in M and $T_x M$ respectively. They are related by the exponential map, Φ_x , as follows: $B(x, r) = \Phi_x(B_x(\mathbf{0}, r))$. We refer to the coordinates obtained in the tangent space by the exponential map Φ as normal coordinates. Using normal coordinates, $B_x(\mathbf{0}, r) \subset T_x M$ is endowed with the Riemannian metric dist_g and measure μ_g . On the other hand, the tangent space $T_x M$ can also be identified with \mathbb{R}^D by choosing an orthonormal basis. This provides Euclidean metric dist_E and measure μ_E on $T_x M$, in particular, on $B_x(\mathbf{0}, r)$. There is a simple relation between μ_E and μ_g (do Carmo, 1992):

$$\mu_g(d\mathbf{y}) = \mu_E(d\mathbf{y}) + \mathcal{O}(r^2)d\mathbf{y} \quad \text{for } \mathbf{y} \in B_x(\mathbf{0}, r). \quad (10)$$

Figure 14 highlights the difference between dist_E and dist_g . It shows the tangent space $T_n \mathbb{S}^2$ of the north pole, n , of \mathbb{S}^2 and the straight blue line connecting $\Phi_n^{-1}(x)$ and $\Phi_n^{-1}(y)$ in T_n ; it is the shortest path w.r.t. dist_E . On the other hand, the shortest path w.r.t. dist_g is clearly the equator (the geodesic

connecting x and y), which is the black arc on $T_n\mathbb{S}^2$; it is different than the blue line. In fact, only lines in $T_n\mathbb{S}^2$ connecting the origin and other points on $T_n\mathbb{S}^2$ correspond to geodesics on \mathbb{S}^2 for a general metric. As a consequence, the measures μ_g and μ_E induced by dist_g and dist_E are also different.

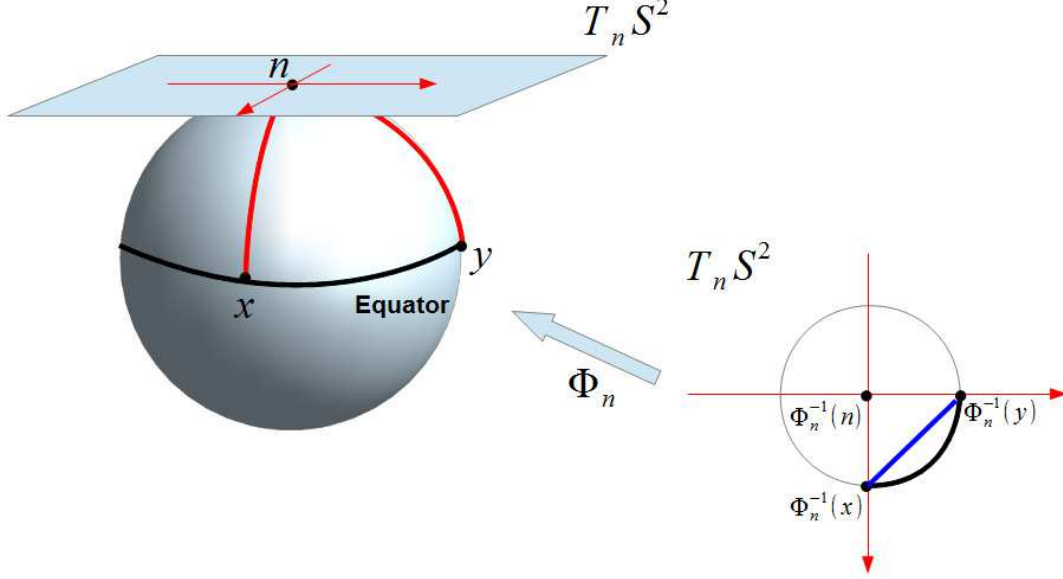


Figure 14: Difference between the metrics dist_g and dist_E on $T_n\mathbb{S}^2$. The black arc in $T_n\mathbb{S}^2$ is a geodesic under the metric g . The blue segment in $T_n\mathbb{S}^2$ is a geodesic under the Euclidean metric dist_E .

Given a submanifold $S \subset M$ (or a τ -tubular neighborhood S^τ of S), the metric tensor on S (or S^τ) inherited from g induces a measure μ_{gS} on S (or S^τ), which is called the uniform measure on S (or S^τ). For simplicity we assume throughout most of the proof that $\tau = 0$ and thus mainly discuss the measure μ_{gS} on S . In Section 5.8 we generalize the proof to the noisy case and thus discuss μ_{gS} on S^τ . The push-forward measure of μ_{gS} by Φ_x^{-1} is a measure on T_xM , which is again denoted by μ_{gS} . By definition, the support of the push-forward measure μ_{gS} is $\Phi_x^{-1}(S)$, which is a submanifold of $T_xM \equiv \mathbb{R}^D$. The Euclidean metric dist_E similarly induces another measure μ_{ES} , which is supported on $\Phi_x^{-1}(S)$.

For a measure μ on T_xM and a subset $H \subset T_xM$ of positive such measure, the expected covariance matrix $\mathbb{E}_\mu \mathbf{C}_H$ is defined by

$$\mathbb{E}_\mu \mathbf{C}_H = \frac{1}{\mu(H)} \int_{\mathbf{y} \in H} \mathbf{y} \mathbf{y}^T \mu(d\mathbf{y}) - \frac{1}{(\mu(H))^2} \int_{\mathbf{y} \in H} \mathbf{y} \mu(d\mathbf{y}) \cdot \int_{\mathbf{y} \in H} \mathbf{y}^T \mu(d\mathbf{y}). \quad (11)$$

For the two compact submanifolds of the model, S_1 and S_2 , we denote $S = S_1 \cup S_2$ and define the following two measures w.r.t. S : $\mu_{gS} = \mu_{gS_1} + \mu_{gS_2}$ and $\mu_{ES} = \mu_{ES_1} + \mu_{ES_2}$. The covariance matrices w.r.t. μ_{gS} and μ_{ES} are denoted by $\mathbb{E}_{\mu_{gS}} \mathbf{C}_H$ and $\mathbb{E}_{\mu_{ES}} \mathbf{C}_H$, respectively. For simplicity, when $H = B_x(\mathbf{0}, r) \subset T_xM$, we denote them by $\mathbb{E}_{\mu_{gS}} \mathbf{C}_x$ and $\mathbb{E}_{\mu_{ES}} \mathbf{C}_x$. For $H = \Phi_z^{-1}(B(x, r)) \subset T_zM$, we denote them by $\mathbb{E}_{\mu_{gS}} \mathbf{C}_x^z$ and $\mathbb{E}_{\mu_{ES}} \mathbf{C}_x^z$.

If a dataset $X \in M$ is given, let \mathbf{C}_{x_0} denote the sample covariance of the data $\Phi_{x_0}^{-1}(B(x_0, r) \cap X)$ on $T_{x_0}M$ and $\mathbf{C}_{x_0}^z$ denote the sample covariance of the data $\Phi_z^{-1}(B(x_0, r) \cap X)$ on T_zM . Let $\theta_{\min}(T_zS_1, T_zS_2)$ denote the minimal nonzero principal angle between the subspaces $T_zS_1, T_zS_2 \subset T_zM^2$ and let

$$\theta_0(S_1, S_2) = \inf_{z \in S_1 \cap S_2} \theta_{\min}(T_zS_1, T_zS_2). \quad (12)$$

²We only use $\theta_{\min}(T_zS_1, T_zS_2)$ when there is a nonzero principal angle. It is thus well-defined.

For $x \in S_1 \cap S_2$, let $\theta_{\max}(T_x S_1, T_x S_2)$ denote the largest principal angle between $T_x S_1$ and $T_x S_2$ and let

$$\theta_{\max}(S_1, S_2) = \min_{x \in S_1 \cap S_2} \theta_{\max}(T_x S_1, T_x S_2). \quad (13)$$

Recall that the notation

$$Q_1(r) = Q_2(r) + \mathcal{O}(r^n)$$

means that there is a constant C independent of r such that

$$|Q_1(r) - Q_2(r)| \leq Cr^n. \quad (14)$$

If $Q_1(r)$ and $Q_2(r)$ are matrices, then (14) applies to their entries. If $x_i, x_j \in M$, we denote by $l'(x_i, x_j)$ the tangent vector of $l(x_i, x_j)$ at x_i (it was denoted by \mathbf{v}_{ij} in Section 2.2). We denote the empirical geodesic angle between x and y by $\theta_{x,y}$ (where for data points x_i, x_j , $\theta_{x_i, x_j} = \theta_{ij}$). Lastly, for a matrix \mathbf{C} , $\lambda_k(\mathbf{C})$ stands for the k th largest eigenvalue of \mathbf{C} .

5.2 A Generative Multi-Geodesic Model

We review in more details the generative model for two geodesic submanifolds (see Section 2.1). We first state the definition of geodesic submanifolds.

Definition 2 *For a Riemannian manifold M , a submanifold S is called a geodesic submanifold if $\forall x, y \in S$, the shortest geodesic connecting x and y in M is also contained in S .*

Let S_1, S_2 be two compact geodesic submanifolds of dimension d in a Riemannian manifold (M, g) and recall that $S = S_1 \cup S_2$. Let S_1^τ, S_2^τ and S^τ denote τ -tubular neighborhoods of S_1, S_2 and S respectively. For example, $S_1^\tau = \{x \in M : \text{dist}_g(x, S_1) \leq \tau\}$, where $\text{dist}_g(x, S_1) := \min_{y \in S_1} \text{dist}_g(x, y)$. The dataset X of size N is i.i.d. sampled from the normalized version of μ_{gS} (by $\mu_{gS}(S^\tau)$) on S^τ . We recall the notation: $X_1 = S_1 \cap X$ and $X_2 = S_2 \cap X$. Fixing a point x_i , then $\mathbf{x}_j^{(i)}$ is i.i.d. sampled from the normalized push-forward μ_{gS} on $T_{x_i} M$.

5.3 Local Concentration with High Probability

We verify here the concentration of the local covariance matrices and the existence of sufficiently large samples in local neighborhoods from the same submanifold. We follow Arias-Castro et al. (2013)³ and define on the probability space S^N (i.e., $(S_1 \cup S_2) \times \dots \times (S_1 \cup S_2)$), the following events Ω_1 and Ω_2 :

$$\Omega_1 = \bigcap_{k=1}^2 \{X = (x_1, \dots, x_N) \in S^N : \#\{i : x_i \in S_k \cap B(y, r/C_\Omega)\} > nr^d/C_7, \forall y \in S_k\}, \quad (15)$$

$$\Omega_2 = \{X = (x_1, \dots, x_N) \in S^N : \|\mathbf{C}_{x_i} - \mathbb{E}_{\mu_{gS}} \mathbf{C}_{x_i}\| \leq r^3, i = 1, \dots, N\}, \quad (16)$$

where C_Ω and C_7 are specified in Arias-Castro et al. (2013) (C_Ω depends on d and θ_0 (defined in (12)) and C_7 depends on the covering number of S) and \mathbf{C}_{x_i} is the sample covariance of images $\{\mathbf{x}_j^{(i)}\}_{j \in J(x_i, r)}$ on $T_{x_i} M$. We note that Ω_1 is the set of datasets of N samples, where each dataset satisfies the following condition: for any point in S_i ($i = 1, 2$ is fixed), there are enough samples that also belong to S_i (their fraction is proportional to r^d). The set Ω_2 is the set of datasets of N samples with sufficient concentration of local covariance matrices. The following theorem of Arias-Castro et al. (2013, page 35) ensures that the event $\Omega = \Omega_1 \cap \Omega_2$ is large. It uses the constant $C_0 = 4d + 2C_7$ and an absolute constant C'_0 .

³For simplicity, we set the parameter t of Arias-Castro et al. (2013) to be equal to r

Theorem 3 Let $\Omega = \Omega_1 \cap \Omega_2$. Then,

$$\mathbb{P}(\Omega^c) \leq C_0 \cdot N e^{-Nr^{d+2}/C'_0}.$$

In view of this theorem, we assume in the rest of the proof that

$$X \in \Omega. \tag{17}$$

5.4 Ensuring Connectedness of X_1^* and X_2^*

The following proposition establishes WLOG the connectedness of the graph of the set X_1^* (defined in (7)). It uses a constant C_1 , which is clarified in the proof and depends on geometric properties of S_1 and S_2 and their angle of intersection.

Proposition 4 *There exists a constant $C_1 > 1$ such that if*

$$r < \frac{\min(\eta, \sigma_a, \sigma_d)}{C_1}, \tag{18}$$

then the graph with nodes at X_1^ and edges given by \mathbf{W} is connected.*

5.4.1 Proof of Proposition 4

Three different constants C_8 , C_9 and C_{10} appear in the proof. As clarified below, they depend on geometric properties of S_1 and S_2 and their angle of intersection. The constant C_1 is then determined by these constants as follows: $C_1 = \max(\{C_i\}_{i=8}^{10})$.

The proof is divided into three parts. The first one shows that $\mathbf{1}_{\dim(T_{x_i}^E S) = \dim(T_{x_j}^E S)} = 1$ for all x_i, x_j in X_1^* if $r < \eta/C_8$. The second one shows that $\mathbf{1}_{(\theta_{ij} + \theta_{ji}) < \sigma_a} = 1$ for all x_i, x_j in X_1^* if $\sigma_a \geq C_9 r$. The last one uses an argument of Arias-Castro et al. (2013, page 38). It claims that the graph with nodes at X_1^* and weights given by the indicator function $\mathbf{1}_{\text{dist}_g(x_i, x_j) < \sigma_d}$ is connected if $r \leq \sigma_d/C_{10}$.

Part I: We prove the following lemma, which clearly implies that $\mathbf{1}_{\dim(T_{x_i}^E S) = \dim(T_{x_j}^E S)} = 1$ for $x_i, x_j \in X_1^*$.

Lemma 5 *There exists a constant $C_8 > 1$ such that if $x_0 \in X_1^*$, $r < \eta/C_8$ and $0 < \eta < 1$, then*

$$\dim(T_{x_0}^E S) = \dim(T_{x_0} S). \tag{19}$$

Proof Recall that \mathbf{C}_{x_0} denotes the sample covariance of the transformed data $\Phi_x^{-1}(X) \cap B_{x_0}(\mathbf{0}, r)$. We denote $H = B_{x_0}(\mathbf{0}, r) \cap T_{x_0} S$ and note that

$$\begin{aligned} \mathbb{E}_{\mu_{gS}} \mathbf{C}_{x_0} &= \frac{1}{\mu_{gS}(H)} \int_H \mathbf{y} \mathbf{y}^T \mu_S(d\mathbf{y}) - \frac{1}{(\mu_{gS}(H))^2} \int_H \mathbf{y} \mu_{gS}(d\mathbf{y}) \cdot \int_H \mathbf{y}^T \mu_S(d\mathbf{y}) \\ &= \frac{1}{\mu_{ES}(H)} \int_H \mathbf{y} \mathbf{y}^T \mu_{IS}(d\mathbf{y}) - \frac{1}{(\mu_{ES}(H))^2} \int_H \mathbf{y} \mu_{ES}(d\mathbf{y}) \cdot \int_H \mathbf{y}^T \mu_{IS}(d\mathbf{y}) + \mathcal{O}(r^4) \\ &= \mathbb{E}_{\mu_{ES}} \mathbf{C}_{x_0} + \mathcal{O}(r^4). \end{aligned} \tag{20}$$

The first and third equalities of (20) follow from the definition of the expected covariance. The second equality of (20) follows from (10) and the fact that $\|\mathbf{y}\| \leq r$. A slight generalization of Lemma 11 of Arias-Castro et al. (2013) implies that

$$\mathbb{E}_{\mu_{ES}} \mathbf{C}_{x_0} = \frac{r^2}{d+2} \mathbf{P}_{T_{x_0} S}, \tag{21}$$

where $\mathbf{P}_{T_{x_0}S}$ is the orthogonal projector onto $T_{x_0}S$ in $T_{x_0}M$. Equation (20) and (21) imply that

$$\|\mathbb{E}_{\mu_{gS}} \mathbf{C}_{x_0} - \frac{r^2}{d+2} \mathbf{P}_{T_{x_0}S}\| < C_S r^4, \quad (22)$$

where $C_S > 0$ is a constant depending on the Riemannian metric g (arising due to (10)). Using this constant C_S , we define

$$C_8 = 2(d+2)(C_S + 1). \quad (23)$$

We note that $C_8 > 1$. Combining this observation with the following two assumptions: $r < \eta/C_8$ and $0 < \eta < 1$, we conclude that $r < 1$.

Combining the triangle inequality, (17), (22) and the fact that $r < 1$, we conclude that

$$\|\mathbf{C}_{x_0} - \frac{r^2}{d+2} \mathbf{P}_{T_{x_0}S}\| \leq \|\mathbf{C}_{x_0} - \mathbb{E}_{\mu_{gS}} \mathbf{C}_{x_0}\| + \|\mathbb{E}_{\mu_{gS}} \mathbf{C}_{x_0} - \frac{r^2}{d+2} \mathbf{P}_{T_{x_0}S}\| < r^3 + C_S r^4 \leq (C_S + 1)r^3. \quad (24)$$

The application of both Weyl's inequality (Stewart and Sun, 1990) and (24) results in the following lower bound of $\lambda_1(\mathbf{C}_{x_0})$ and upper bound of $\lambda_{d+1}(\mathbf{C}_{x_0})$:

$$\lambda_{d+1}(\mathbf{C}_{x_0}) < (C_S + 1)r^3 \quad \text{and} \quad \lambda_1(\mathbf{C}_{x_0}) > \frac{r^2}{d+2} - (C_S + 1)r^3. \quad (25)$$

It follows from (23), (25) and elementary algebraic manipulations that

$$\begin{aligned} \frac{\lambda_{d+1}(\mathbf{C}_{x_0})}{\lambda_1(\mathbf{C}_{x_0})} &< \frac{(C_S + 1)r^3}{\frac{r^2}{d+2} - (C_S + 1)r^3} = \frac{C_S + 1}{1/(r(d+2)) - (C_S + 1)} \\ &< \frac{C_S + 1}{C_8/(d\eta + 2\eta) - (C_S + 1)} = \frac{\eta}{2 - \eta} < \eta. \end{aligned} \quad (26)$$

Equation (19) thus follows from (26) and the thresholding of eigenvalues by $\eta\|\mathbf{C}_{x_0}\|$ in Algorithm 1. \blacksquare

Part II: Next, we prove that $\mathbf{1}_{(\theta_{ij} + \theta_{ji}) < \sigma_a} = 1$ if $\sigma_a \geq C_9 r$.

Lemma 6 *There exists a constant $C_9 > 1$ such that if $x, y \in X_1^*$ and*

$$\sigma_a \geq C_9 r, \quad (27)$$

then $\mathbf{1}_{(\theta_{x,y} + \theta_{y,x}) < \sigma_a} = 1$.

Proof We define

$$C_9 = \sqrt{2}(C_S + 1)(d+2)\pi, \quad (28)$$

where C_S is the constant introduced in (22). We show that for $x, y \in X_1^*$:

$$\theta_{x,y} < \frac{C_9}{2} r, \quad (29)$$

which immediately implies the lemma.

In order to prove (29), we first apply the Davis-Kahan Theorem (Davis and Kahan, 1970) and (19) and then apply (24) to obtain the following bound on the distance between the subspaces $T_x^E S$ and $T_x S$ (which are spanned by the top d eigenvectors of \mathbf{C}_x and $\frac{r^2}{d+2} \mathbf{P}_{T_x S}$, respectively; this observation uses (19)):

$$\|\mathbf{P}_{T_x^E S} - \mathbf{P}_{T_x S}\| < \frac{\sqrt{2}\|\mathbf{C}_x - \frac{r^2}{d+2} \mathbf{P}_{T_x S}\|}{\frac{r^2}{d+2}} < \sqrt{2}(C_S + 1)(d+2)r. \quad (30)$$

We remark that in applying the Davis-Kahan Theorem we made use of the following basic calculation of Δ , the d th spectral gap of $\frac{r^2}{d+2}\mathbf{P}_{T_x S}$: $\Delta = \lambda_d(\frac{r^2}{d+2}\mathbf{P}_{T_x S}) - \lambda_{d+1}(\frac{r^2}{d+2}\mathbf{P}_{T_x S}) = \frac{r^2}{d+2}$.

Next, we recall that $\theta_{\max}(T_x^E S, T_x S)$ denotes the largest principal angle between $T_x^E S$ and $T_x S$. We note that Lemma 15 of Arias-Castro et al. (2013) (whose application requires (19)), (30), (28) and Jordan's inequality (lower bounding the sin function by $2/\pi$) imply that

$$\theta_{\max}(T_x^E S, T_x S) = \sin^{-1}(\|\mathbf{P}_{T_x^E S} - \mathbf{P}_{T_x S}\|) < \sin^{-1}(\sqrt{2}(C_S + 1)(d+2)r) < \frac{C_9}{2}r. \quad (31)$$

Since $\theta_{x,y}$ is the angle between $l'(x,y) \in T_x S$ and $T_x^E S$, (29) follows from (31). We can then conclude that if $\sigma_a \geq C_9 r$, then $\mathbf{1}_{(\theta_{ij} + \theta_{ji}) < \sigma_a} = 1$ for all x_i, x_j in X_1^* . ■

Part III: By the construction of the affinity matrix \mathbf{W} and Lemmata 5 and 6, the connectivity between points $x_i, x_j \in X_1^*$ is solely determined by the indicator function $\mathbf{1}_{\text{dist}_g(x_i, x_j) < \sigma_d}$. It is obvious that if $\sigma_d > 4r$ then the graph with nodes in X_1 and weights $\mathbf{1}_{\text{dist}_g(x_i, x_j) < \sigma_d}$ is connected (this can be done by finite covering of S_1 with balls of radius r). It follows from Arias-Castro et al. (2013, pages 38-39) that the graph with nodes in X_1^* is also connected if

$$r \leq \sigma_d / C_{10}. \quad (32)$$

There is one component in the argument of Arias-Castro et al. (2013, page 38) that requires careful adaptation to the Riemannian case. It is related to the determination of the constant C_{10} . This constant is set to be $(3C' + 9)^{-1}$ (see Arias-Castro et al. (2013, page 39)). In the Euclidean case, C' is guaranteed by Lemma 18 of Arias-Castro et al. (2013). The adaptation of this Lemma to the Riemannian case can be stated in the following lemma (it uses θ_0 , which was defined in (12)).

Lemma 7 *Let (M, g) be a Riemannian manifold and S_1, S_2 be two compact geodesic submanifolds of dimension d such that $\theta_0(S_1, S_2) > 0$. Then there is a constant C' such that*

$$\text{dist}_g(x, S_1 \cap S_2) \leq C' \max\{\text{dist}_g(x, S_1), \text{dist}_g(x, S_2)\} \quad \forall x \in S_1 \cup S_2.$$

We prove Lemma 7 in Appendix D.1. The proof implies that C' is determined by the geometric properties of S_1 and S_2 and the angle $\theta_0(S_1, S_2)$.

5.5 Disconnectedness Between \hat{X}^c and X_1^* (or X_2^*)

We show here that the points in \hat{X}^c (where \hat{X} is defined in (8)) are not connected to the points of X^* . In Section 5.4, we showed that the estimated dimensions of local neighborhoods of points in X^* equal d . In this section, we show that the estimated dimensions of local neighborhoods of points in \hat{X}^c are larger than d . Since $\mathbf{1}_{\dim(T_{x_i}^E S) = \dim(T_{x_j}^E S)}$ is a multiplicative term of \mathbf{W} , we conclude that \hat{X}^c is disconnected from X^* . The following main proposition of this section implies that WLOG the estimated tangent dimension at $\hat{X}^c \cap X_1$ is at least $d+1$ (it uses the angle $\theta_{\max}(S_1, S_2)$ defined in (13)).

Proposition 8 *There exists a constant $C_2 > 1$ depending only on d and $\theta_{\max}(S_1, S_2)$ such that if $r < \eta$,*

$$\eta < C_2^{-\frac{d+2}{2}}, \quad (33)$$

$$\delta := r \sqrt{1 - C_2 \eta^{\frac{2}{d+2}}} \quad (34)$$

and

$$x \in \hat{X}^c \cap X_1, \text{ that is, } \text{dist}_g(x, S_2) < \delta, \quad (35)$$

then

$$\frac{\lambda_{d+1}(\mathbf{C}_x)}{\lambda_1(\mathbf{C}_x)} > \eta.$$

Proof Let us first sketch the idea of the proof. It is easier to estimate the local covariance matrices when the two manifolds are subspaces (see Lemma 21 of Arias-Castro et al. (2013)). However, for $x \in \hat{X}^c \cap X_1$, the logarithm map of S into $T_x M$ does not result in two subspaces (see Figure 15). On the other hand, for z , the projection of x onto $S_1 \cap S_2$, the logarithm map of S into $T_z M$ results in two subspaces, where the local covariance can be estimated more easily. Some difficulties arise due to the application of the logarithm map and the change of tangent spaces. In particular, the ball $B(x, r)$ becomes irregular in the domain $T_z M$.

We recall that $\mu_{gS} = \mu_{gS_1} + \mu_{gS_2}$ and $\mu_{ES} = \mu_{ES_1} + \mu_{ES_2}$. We arbitrarily fix $x_0 \in S_1$ such that $\text{dist}_g(x_0, S_2) < r$. We note that Lemma 7 implies that

$$\text{dist}_g(x_0, S_1 \cap S_2) \leq Cr. \quad (36)$$

Let

$$z = \text{argmin}_{y \in S_1 \cap S_2} \text{dist}_g(x_0, y),$$

where if argmin is not uniquely defined, then z is arbitrarily chosen among all minimizers. It follows from (36) that $\text{dist}_g(x_0, z) \leq Cr$ and from this and the triangle inequality, it follows that

$$B(x_0, r) \subset B(z, (C+1)r). \quad (37)$$

Recall that Φ_{x_0} and Φ_z denote the normal coordinate charts around x_0 and z respectively (see Figure 15); it is sufficient to restrict them to $B(x_0, r)$ and $B(z, (C+1)r)$ respectively. When using the chart Φ_z , S_1 and S_2 correspond to two subspaces in $T_z M$, which we denote by L_1 and L_2 respectively. On the other hand, when using the chart Φ_{x_0} , S_2 corresponds to a manifold in $T_{x_0} M$, whereas S_1 still corresponds to a subspace. It follows from (37) and the invertibility of Φ_z that the composition map $\phi = \Phi_z^{-1} \circ \Phi_{x_0}$ embeds $B_{x_0}(\mathbf{0}, r)$ into $B_z(\mathbf{0}, (C+1)r)$ as shown in Figure 15. Recall that \mathbf{C}_{x_0} denotes the sample covariance of the data $\Phi_{x_0}^{-1}(B(x_0, r) \cap X)$ in $T_{x_0} M$ and $\mathbf{C}_{x_0}^z$ denotes the sample covariance of the data $\Phi_z^{-1}(B(x_0, r) \cap X)$ in $T_z M$. Using the notation $O(D)$ for the set of orthogonal $D \times D$ matrices, we claim that

$$\exists \mathbf{R} \in O(D) \text{ s.t. } \mathbf{R} (\mathbb{E}_{\mu_{gS}} \mathbf{C}_{x_0}) \mathbf{R}^T = \mathbb{E}_{\mu_{gS}} \mathbf{C}_{x_0}^z + \mathcal{O}(r^3). \quad (38)$$

The technical proof of (38) is in Appendix D.2.

We estimate $\mathbb{E}_{\mu_{gS}} \mathbf{C}_{x_0}^z$ as follows. Let $H = \Phi_z^{-1}(B(x_0, r) \cap (S_1 \cup S_2))$ and $H' = B_I(\Phi_z^{-1}(x_0), r) \cap (L_1 \cup L_2)$ (see Figure 16), where $B_I(\Phi_z^{-1}(x_0), r)$ is the r -ball with center $\Phi_z^{-1}(x_0)$ in $T_z M$, which uses the Euclidean distance dist_E .

The rest of the proof requires the following two technical observations

$$\mu_{ES}((H \setminus H') \cup (H' \setminus H)) = \mathcal{O}(r) \mu_{ES}(H). \quad (39)$$

and

$$\mathbb{E}_{\mu_{gS}} \mathbf{C}_{x_0}^z = \mathbb{E}_{\mu_{ES}} \mathbf{C}_{x_0}^z + \mathcal{O}(r^3) = \mathbb{E}_{\mu_{ES}} \mathbf{C}_{H'} + \mathcal{O}(r^3). \quad (40)$$

We prove (39) in Appendix D.3. The first equality of (40) follows from the definition of the expected covariance (see (11)), (10) and the fact that $\|\mathbf{y}\| \leq (C+1)r$. The second equality of (40) follows from the definition of the expected covariance (see (11)), (39) and the fact that $\|\mathbf{y}\| \leq (C+1)r$.

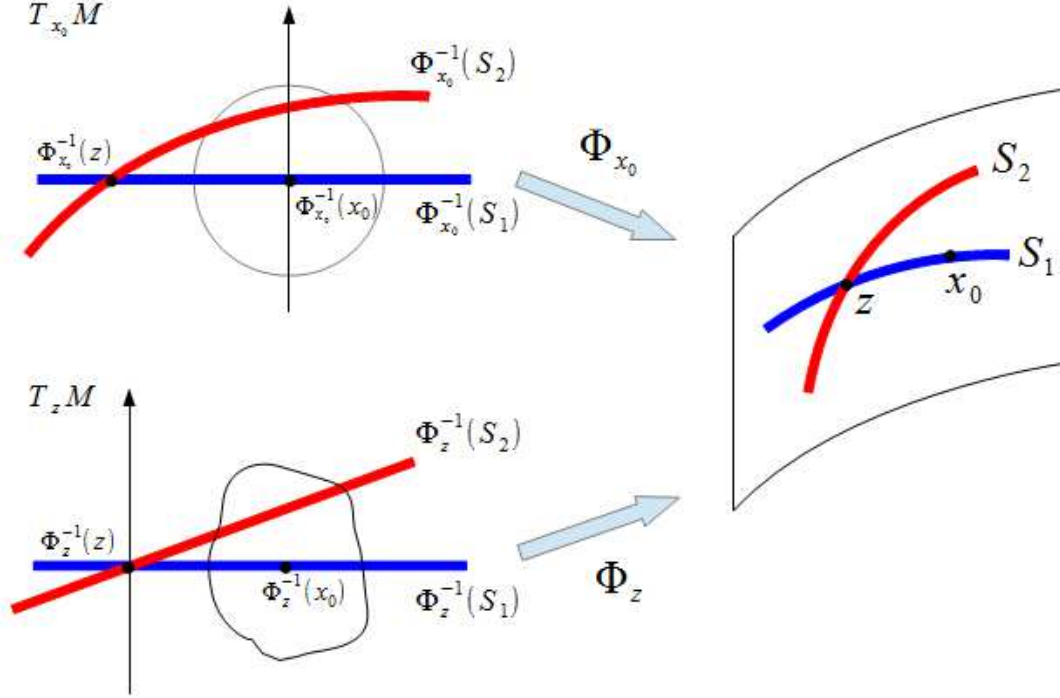


Figure 15: The transition map between normal coordinates of $T_{x_0}M$ and T_zM . Notice the regular ball $B_{x_0}(\mathbf{0}, r)$ in $T_{x_0}M$ is mapped to the irregular region in T_zM because the exponential maps Φ_{x_0} and Φ_z are nonlinear.

It follows from (16), (17), (38), (40) and the triangle inequality that

$$\begin{aligned} \|\mathbf{R}\mathbf{C}_{x_0}\mathbf{R}^T - \mathbb{E}_{\mu_{ES}} \mathbf{C}_{H'}\| &\leq \|\mathbf{R}\mathbf{C}_{x_0}\mathbf{R}^T - \mathbf{R}\mathbb{E}_{\mu_{gS}} \mathbf{C}_{x_0}\mathbf{R}^T\| + \|\mathbf{R}\mathbb{E}_{\mu_{gS}} \mathbf{C}_{x_0}\mathbf{R}^T - \mathbb{E}_{\mu_{ES}} \mathbf{C}_{x_0}^z\| + \\ &\quad \|\mathbb{E}_{\mu_{ES}} \mathbf{C}_{x_0}^z - \mathbb{E}_{\mu_{ES}} \mathbf{C}_{H'}\| \leq r^3 + \mathcal{O}(r^3) + \mathcal{O}(r^3) \leq C'_S r^3 \end{aligned} \quad (41)$$

for a constant $C'_S > 0$.

The combination of (41), Weyl's inequality (Stewart and Sun, 1990) for $\mathbf{R}(\mathbf{C}_{x_0})\mathbf{R}^T$ and $\mathbb{E}_{\mu_{ES}} \mathbf{C}_{H'}$, and the fact that $\mathbf{R}\mathbf{C}_{x_0}\mathbf{R}^T$ and \mathbf{C}_{x_0} have the same eigenvalues implies that

$$\lambda_{d+1}(\mathbf{C}_{x_0}) \geq \lambda_{d+1}(\mathbb{E}_{\mu_{ES}} \mathbf{C}_{H'}) - C'_S r^3, \quad \lambda_1(\mathbf{C}_{x_0}) \leq \lambda_1(\mathbb{E}_{\mu_{ES}} \mathbf{C}_{H'}) + C'_S r^3. \quad (42)$$

Notice that $\theta_{\max}(S_1, S_2) \leq \theta_{\max}(L_1, L_2)$ by definition. Applying (42) and Lemma 21 of Arias-Castro et al. (2013) to $\mathbb{E}_{\mu_{ES}} \mathbf{C}_{H'}$, where $\theta_{\max}(L_1, L_2)$ is replaced by $\theta_{\max}(S_1, S_2)$ and proper scaling is used, results in

$$\begin{aligned} \frac{\lambda_{d+1}(\mathbf{C}_{x_0})}{\lambda_1(\mathbf{C}_{x_0})} &\geq \frac{\frac{1}{8(d+2)}(1 - \cos \theta_{\max}(S_1, S_2))^2(1 - (\text{dist}_g(x_0, S_2)/r)^2)_+^{d/2+1} - C'_S r^3}{1/(d+2) + (\text{dist}_g(x_0, S_2)/r)(1 - (\text{dist}_g(x_0, S_2)/r)^2)_+^{d/2} + C'_S r^3} \\ &\geq \frac{\frac{1}{8(d+2)}(1 - \cos \theta_{\max}(S_1, S_2))^2(1 - (\text{dist}_g(x_0, S_2)/r)^2)_+^{d/2+1} - C'_S r^3}{1/(d+2) + 1 + C'_S r^3}. \end{aligned} \quad (43)$$

We remark that the second inequality of (43) is derived by applying the bound: $\text{dist}_g(x, S_2) < r$. In order to satisfy $\frac{\lambda_{d+1}(\mathbf{C}_{x_0})}{\lambda_1(\mathbf{C}_{x_0})} > \eta$, we require that

$$\frac{\frac{1}{8(d+2)}(1 - \cos \theta_{\max}(S_1, S_2))^2(1 - (\text{dist}_g(x_0, S_2)/r)^2)_+^{d/2+1} - C'_S r^3}{1/(d+2) + 1 + C'_S r^3} > \eta. \quad (44)$$

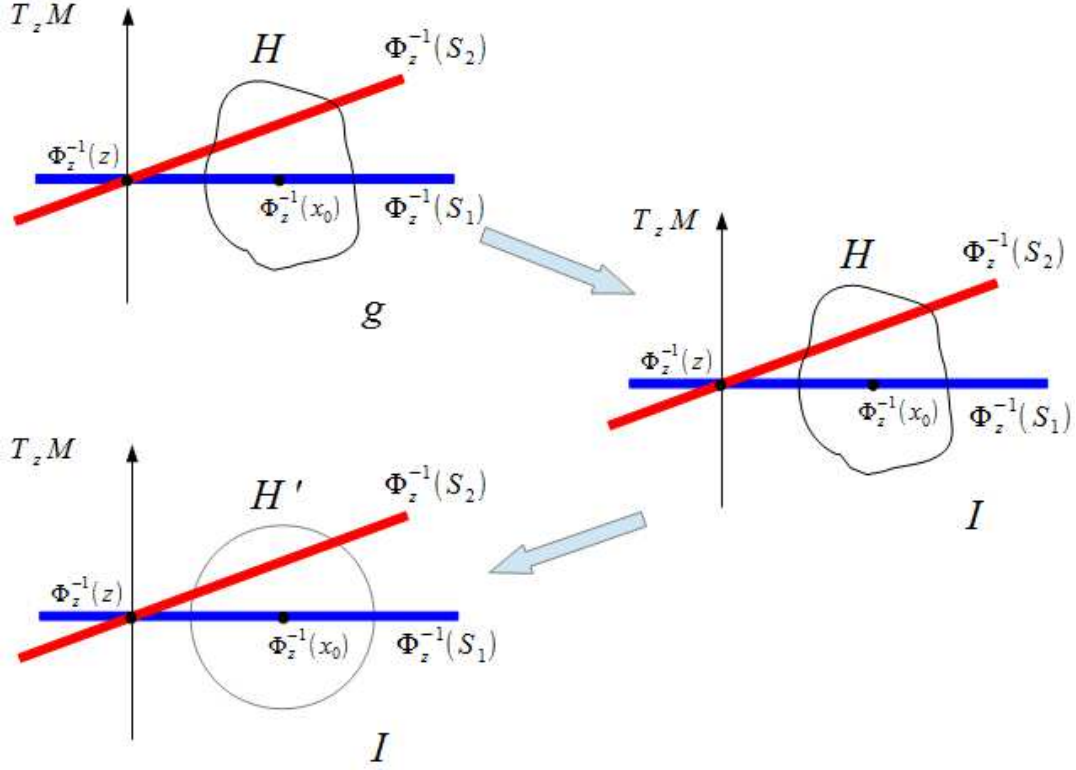


Figure 16: Change of domain and metric

Since $r < \eta < 1$, we replace $C'_S r^3$ with $C'_S \eta$ in the numerator of (44) and $C'_S r^3$ with C'_S in the denominator of (44) and slightly simplify the inequality to obtain the following stronger requirement:

$$\frac{(1 - \cos \theta_{\max}(S_1, S_2))^2}{8(d+2)} (1 - (\text{dist}_g(x_0, S_2)/r)^2)^{d/2+1} > \left(\frac{1}{d+2} + 1 + 2C'_S \right) \eta. \quad (45)$$

Finally, setting

$$C_2 = \left(\frac{8d + 24 + 16(d+2)C'_S}{(1 - \cos \theta_{\max}(S_1, S_2))^2} \right)^{\frac{2}{d+2}} \quad (46)$$

we can rewrite (45) as follows

$$(1 - (\text{dist}_g(x_0, S_2)/r)^2)^{\frac{d+2}{2}} > C_2^{\frac{d+2}{2}} \eta. \quad (47)$$

We immediately conclude (47) (and consequently the lemma) from (34) and (35). \blacksquare

We end this section with an immediate corollary of Proposition 8, which is crucial in order to follow the proof.

Corollary 9 *The following relations are satisfied:*

$$X_1^* \subset \hat{X}_1 \quad \text{and} \quad X_2^* \subset \hat{X}_2.$$

Proof It follows from Lemma 5 and Proposition 8 that $X_1^* \cap \hat{X}^c = \emptyset$. Therefore $X_1^* \subset \hat{X}_1$. Similarly, $X_2^* \subset \hat{X}_2$. \blacksquare

5.6 The Disconnectedness of X_1^* and X_2^*

We show here that the graphs with nodes at X_1^* and X_2^* are disconnected. The idea is to show that the function $\mathbf{1}_{\text{dist}_g(x_i, x_j) < \sigma_d} \mathbf{1}_{\theta_{ij} + \theta_{ji} < \sigma_a}$ (and thus the weight \mathbf{W}) is zero between two points in $\hat{X}_1 \supset X_1^*$ and $\hat{X}_2 \supset X_2^*$ for appropriate choice of constants. This and Proposition 8 imply that the graphs associated with X_1^* and X_2^* are disconnected. We first establish a lower bound on the empirical geodesic angle in Lemma 10 and then conclude that there is no direct connection between the sets \hat{X}_1 and \hat{X}_2 in Corollary 11.

Lemma 10 *There exist constants $C_3 > 0$ and $C_4 > 0$ such that if $x_1 \in \hat{X}_1$, $x_2 \in \hat{X}_2$,*

$$\text{dist}_g(x_1, x_2) < \sigma_d, \quad (48)$$

$$\text{and } \sigma_d < C_4^{-\frac{1}{2}}, \quad (49)$$

then the angle between the estimated tangent subspace $T_{x_1}^E S_1$ and the line segment $l_{12}^{(1)}$, which connects the origin and $\mathbf{x}_2^{(1)}$ (the image of x_2 by \log_{x_1}) in $T_{x_1} M$ is bounded below as follows:

$$\angle(l_{12}^{(1)}, T_{x_1}^E S_1) > \min(\sin^{-1}(\delta/2\sigma_d) - C_3\eta^{d/(d+2)} - C_3r, \pi/6). \quad (50)$$

Proof The proof develops various geometric estimates that eventually conclude (50). Let

$$\mathbf{x}_3 = \text{argmin}_{\mathbf{x} \in T_{x_1} S_1} \text{dist}_g(\mathbf{x}, \mathbf{x}_2^{(1)}) \quad \text{and} \quad \mathbf{x}_4 = \text{argmin}_{\mathbf{x} \in T_{x_1} S_1} \text{dist}_E(\mathbf{x}, \mathbf{x}_2^{(1)}),$$

where dist_E is defined with respect to the normal coordinate chart in $T_x M$ (see Figure 17).

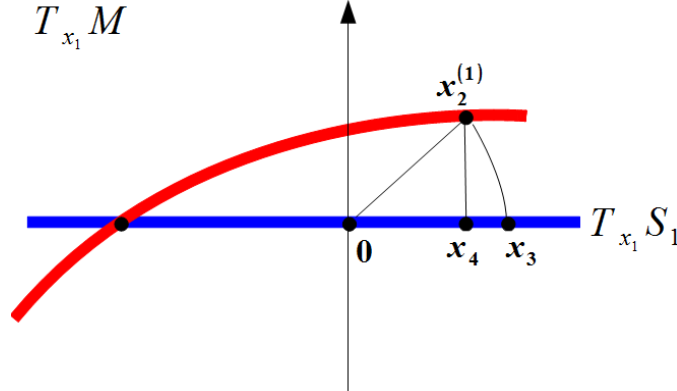


Figure 17: The normal coordinate chart at x_1

We note that by definition \mathbf{x}_4 is the projection of $\mathbf{x}_2^{(1)}$ onto $T_{x_1} S_1$ and thus

$$\text{dist}_E(\mathbf{x}_4, \mathbf{0}) < \text{dist}_g(\mathbf{x}_2^{(1)}, \mathbf{0}). \quad (51)$$

Combining (51) with the fact that dist_E and dist_g are the same on lines through the origin in $T_{x_1} M$ and then applying (48), we obtain that

$$\text{dist}_g(\mathbf{x}_4, \mathbf{0}) < \text{dist}_g(\mathbf{x}_2^{(1)}, \mathbf{0}) < \sigma_d. \quad (52)$$

Furthermore, combining the following two facts: \mathbf{x}_3 is a minimizer of $\text{dist}_g(\cdot, \mathbf{x}_2^{(1)}) \in T_{x_1} S_1$ and $x_2 \in \hat{X}_2$, we obtain that

$$\delta \leq \text{dist}_g(x_2, \Phi_{x_1}(\mathbf{x}_3)) = \text{dist}_g(\mathbf{x}_2^{(1)}, \mathbf{x}_3) < \text{dist}_g(\mathbf{x}_2^{(1)}, \mathbf{x}_4). \quad (53)$$

We prove in Appendix D.4 that there exists a constant $C_4 > 0$, which depends only on the Riemannian manifold M , such that

$$\forall R > 0, \mathbf{x}, \mathbf{y} \in B_{x_1}(\mathbf{0}, R), \quad |\text{dist}_E(\mathbf{x}, \mathbf{y}) - \text{dist}_g(\mathbf{x}, \mathbf{y})| < C_4 R^2 \text{dist}_E(\mathbf{x}, \mathbf{y}). \quad (54)$$

Applying (54) (with $R = \sigma_d$) first and (53) next we obtain that

$$\begin{aligned} \text{dist}_E(\mathbf{x}_2^{(1)}, \mathbf{x}_4) &> \text{dist}_g(\mathbf{x}_2^{(1)}, \mathbf{x}_4) - C_4 \sigma_d^2 \text{dist}_E(\mathbf{x}_2^{(1)}, \mathbf{x}_4) \\ &> \delta - C_4 \sigma_d^2 \text{dist}_E(\mathbf{x}_2^{(1)}, \mathbf{x}_4) \end{aligned} \quad (55)$$

and consequently

$$\text{dist}_E(\mathbf{x}_2^{(1)}, \mathbf{x}_4) > \frac{\delta}{1 + C_4 \sigma_d^2}. \quad (56)$$

It follows from (49) and (56) that

$$\sin(\angle(l_{12}^{(1)}, T_{x_1} S_1)) = \frac{\text{dist}_E(\mathbf{x}_2^{(1)}, \mathbf{x}_4)}{\text{dist}_E(\mathbf{x}_2^{(1)}, \mathbf{0})} > \frac{\delta}{\sigma_d + C_4 \sigma_d^3} > \delta/2\sigma_d. \quad (57)$$

Our proof concludes from (57) and the following two claims:

$$\sin(\theta_{\max}(T_{x_1}^E S_1, T_{x_1} S_1)) \leq C_3' \eta^{d/(d+2)} + C_3' r \quad (58)$$

and

$$\angle(l_{12}^{(1)}, T_{x_1}^E S_1) \geq \min(\angle(l_{12}^{(1)}, T_{x_1} S_1) - \frac{2\pi\sqrt{d}}{3} \sin(\theta_{\max}(T_{x_1}^E S_1, T_{x_1} S_1)), \pi/6). \quad (59)$$

Inequalities (58) and (59) are verified in Appendices D.5 and D.6 respectively, where we also carefully analyze how the constant C_3' depends on the underlying Riemannian manifold (see (102)). Combining (57), (58) and (59), we conclude (50) by letting $C_3 = \frac{2\pi\sqrt{d}}{3} C_3'$. ■

The desired disconnectedness of X_1^* and X_2^* immediately follows from Lemma 10 in the following way:

Corollary 11 *The graphs with nodes at X_1^* and X_2^* respectively and weights in \mathbf{W} are disconnected if the angle threshold σ_a is chosen such that*

$$\sigma_a < \min(\sin^{-1}(\delta/2\sigma_d) - C_3 \eta^{d/(d+2)} - C_3 r, \pi/6) \quad (60)$$

and the distance threshold σ_d satisfies (49).

Proof When σ_a and σ_d satisfy (60) and (49) respectively, Lemma 10 implies that if $x_i \in \hat{X}_1$ and $x_j \in \hat{X}_2$, then $\mathbf{1}_{\text{dist}_g(x_i, x_j) < \sigma_d} \mathbf{1}_{\theta_{ij} + \theta_{ji} < \sigma_a} = 0$. In other words, there is no direct connection between X_1^* and X_2^* through \hat{X} . On the other hand, Lemma 5 and Proposition 8 imply that X_1^* and X_2^* cannot be connected through points in \hat{X}^c (since points in X^* and \hat{X}^c have different local estimated dimensions). We thus conclude that X_1^* and X_2^* are disconnected. ■

5.7 Conclusion of Theorem 1 for the Noiseless Multi-Geodesic Model

Due to Theorem 3 we replace X with $X \cap \Omega$ and obtain a statement for X with probability at least $1 - C_0 \cdot N e^{-N\tau^{d+2}/C'_0}$. Proposition 4 and Corollary 11 imply that (with probability at least $1 - C_0 \cdot N e^{-N\tau^{d+2}/C'_0}$) X^* has two connected components. They require that the parameters of TGCT satisfy (18), (49) and (60). Additional requirement is specified in (33) (in Proposition 8 which implies Corollary 11). We also note that the requirement $r < \eta < 1$, which also appears in some of the auxiliary lemmata, follows from (18), (33) and the fact that $C_1 > 1$ and $C_2 > 1$. These requirements, i.e., (18), (33), (49) and (60), are sufficient and equivalent to (2) when $\tau = 0$.

Next, we explain why one can choose parameters that satisfy these requirements at the end of this section. The only problem is to make sure that the last inequality of (2) (equivalently, (60)) is satisfied. Given a sufficiently small $r > 0$ satisfying (18), we let $\sigma_a = \alpha r$ for some fixed $\alpha > 0$. The RHS of (60) tends to $\min(\sin^{-1}(\frac{1}{2\alpha}), \pi/6)$ as r and η approach zero. We note that the lower bound of σ_a is $C_1 r$. Therefore, if r and η are sufficiently small so that $\min(\sin^{-1}(1/2\alpha), \pi/6)/2$ is lower than the RHS of (60) and $C_1 r < \min(\sin^{-1}(1/2\alpha), \pi/6)/2$, then σ_a can be chosen from the interval $[C_1 r, \min(\sin^{-1}(1/2\alpha), \pi/6)/2]$.

In order to conclude the proof in this case we upper bound the expected portion of points $\#X^{*c}/\#X$, where $\#X^{*c}$ and $\#X$ denote the cardinality of X^{*c} and X respectively. For this purpose we use the set $X_{S_1 \cap S_2} \supset X^{*c}$, which was defined in (9) in the following way:

$$\begin{aligned} \mathbb{E} \left(\frac{\#X^{*c}}{\#X} \right) &\leq \mathbb{E} \left(\frac{\#X_{S_1 \cap S_2}}{\#X} \right) = \frac{\mu_{gS}(\{x \in S_1 \mid \text{dist}_g(x, S_2) < r\})}{\mu_{gS}(S)} + \\ &\frac{\mu_{gS}(\{x \in S_2 \mid \text{dist}_g(x, S_1) < r\})}{\mu_{gS}(S)} \leq \frac{\mu_{gS}(\{x \in S_1 \cup S_2 \mid \text{dist}_g(x, S_1 \cap S_2) \leq C'r\})}{\mu_{gS}(S)} \\ &\leq C_6 r^{d-\dim(S_1 \cap S_2)}. \end{aligned} \tag{61}$$

The first equality of (61) follows from the fact that the dataset X is i.i.d. sampled from μ_{gS} . The second inequality of (61) follows from Lemma 7. The last one follows from Theorem 1.3 in Gray (1982), where C_6 is a constant depending only on the geometry of the underlying generative model (e.g., the mean curvature and volume of $S_1 \cap S_2$).

5.8 Conclusion of Theorem 1 for the Noisy Multi-Geodesic Model

The above analysis also applies when the generative multi-geodesic model has noise level τ and τ is sufficiently smaller than r , that is,

$$\tau < C_5 r, \tag{62}$$

where $C_5 \ll 1$. Indeed, in this case the estimates of tangent spaces and geodesics are sufficiently close to the estimates without noise. The only difference is that the last bound in (61) has to be replaced with $C_6(r + \tau)^{d-\dim(S_1 \cap S_2)}$. This requires though a sufficiently small noise level (set by C_5). Precise bound on τ is not trivial. Furthermore, the analysis employed here is not optimal. We can thus only claim in theory robustness to very small levels of noise, whereas robustness to higher levels of noise is studied in the experiments.

6 Conclusions

Aiming at efficiently organizing data embedded in a non-Euclidean space according to low-dimensional structures, the present paper studied multi-manifold modeling in such spaces. The paper solves this clustering (or modeling) problem by proposing the novel GCT algorithm. GCT thoroughly exploits the

geometry of the data to build a similarity matrix that can effectively cluster the data (via spectral clustering) even when the underlying submanifolds intersect or have different dimensions. In particular, it introduces the novel idea in non-Euclidean multi-manifold modeling of using directional information from local tangent spaces to avoid neighboring points of clusters different than that of the query point. Theoretical guarantees for successful clustering were established for a variant of GCT, namely TGCT for the MGM setting, which is a non-Euclidean generalization of the widely-used framework of hybrid-linear modeling. Unlike TGCT, GCT combined directional information from local tangent spaces with sparse coding, which aims to improve the clustering result by the use of more succinct representations of the underlying low-dimensional structures and by increasing robustness to corruption. Geodesic information is only used locally and thus in practice the algorithm can fit well in practice to MMM and not MGM. Validated against state-of-the-art existing methods for the non-Euclidean setting, GCT exhibited notable performance in clustering accuracy. More specifically, the paper tested GCT on synthetic and real data of deformed images clustering, action identification in video sequences, brain fiber segmentation in medical imaging and dynamic texture clustering.

7 Acknowledgments

This work was supported by the Digital Technology Initiative, a seed grant program of the Digital Technology Center, University of Minnesota, NSF awards DMS-09-56072, DMS-14-18386 and Eager-13-43860, the University of Minnesota Doctoral Dissertation Fellowship Program, and the Feinberg Foundation Visiting Faculty Program Fellowship of the Weizmann Institute of Science.

A Competing Clustering Algorithms and Their Implementation Details

Section A.1 reviews the competing methods of GCT (in the Riemannian setting) and Section A.2 describes the implementation of both GCT and the competing algorithms, in particular, the choice of all parameters.

A.1 Review of Competing Algorithms

The first competing algorithm is sparse manifold clustering (SMC). This algorithm was first suggested by Elhamifar and Vidal (2011) for clustering submanifolds embedded in Euclidean spaces and later modified by Cetingul et al. (2014) for clustering submanifolds of the sphere. We adapt it to the current setting of clustering submanifolds of a Riemannian manifold and still refer to it as SMC. Its basic idea is as follows: For each data-point x , a local neighborhood is mapped to the tangent space $T_x M$ by the logarithm map and a sparse coding task is solved in $T_x M$ to provide weights for the spectral-clustering similarity matrix.

The second competing algorithm is spectral clustering with Riemannian metric (SCR) by Goh and Vidal (2008). It applies spectral clustering with the weight matrix W whose entries are $\mathbf{W}_{ij} = e^{-\text{dist}_g^2(x_i, x_j)/(2\sigma^2)}$ (see page 4 of Goh and Vidal (2008)). That is, it replaces the usual Euclidean metric in standard spectral clustering with the Riemannian one.

The third competing scheme is the embedded K-means. It embeds the given dataset, which lies on a Riemannian manifold, into a Euclidean spaces (as explained next) and then applies the classical K-means to the embedded dataset. In the experiments, Grassmannian manifolds are embedded by a well-known isometric embedding into Euclidean space (Basri et al., 2011); the manifolds of symmetric $n \times n$ PD matrices are embedded by vectorizing their elements into elements of $\mathbb{R}^{\binom{n+1}{2}}$; and data in the sphere \mathbb{S}^D is already embedded in \mathbb{R}^{D+1} .

A.2 Implementation Details for All Algorithms

GCT follows the scheme of Algorithm 2. For all algorithms, the number K of clusters was known in all experiments. The input parameters of GCT are set as follows: The neighborhood radius r at a point x is chosen to be the average distance of x to its n th nearest point over all x , where $n \in \{15, 16, \dots, 30\}$; the distance and angle thresholds σ_d and σ_a are set to 1 in all experiments (we did not notice a big difference of the results when their values are changed). The dimension of the local tangent space is determined by the largest gap of eigenvalues of each local covariance matrix (more precisely, it is the number of eigenvalues until this gap).

Since there are no online available codes for SMC, SCR and EKM, we wrote our own implementations and will post them (as well as our implementation of GCT) on the supplemental webpage when the paper is accepted for publication. The spectral clustering code in GCT, SMC and SCR, as well as the K -means code in EKM are taken from the implementations of Nikvand (2013). To make a faithful comparison, the input parameter r of SMC is the same as GCT (in particular, we use the radius of neighborhood and not the number of neighbors). SMC also implicitly sets $\sigma_d = 1$. There are no other parameters for SMC. We remark that Elhamifar and Vidal (2011) formed the weight matrix \mathbf{W} as follows: $\mathbf{W}_{ij} = |\mathbf{S}_{ij}| + |\mathbf{S}_{ji}|$, where $|\mathbf{S}_{ij}|$ and $|\mathbf{S}_{ji}|$ are the sparse coefficients. However, this weight was unstable in some experiments and above a certain level of noise SMC often collapsed in some of the random repetition of the experiments. In such cases, we used instead (for all repetitive experiments for the same data set) the weights $\mathbf{W}_{ij} = \exp(|\mathbf{S}_{ij}| + |\mathbf{S}_{ji}|)$ suggested in Cetingul et al. (2014) (which are similar to the ones of GCT). In the case of no collapse with the former weights, we tried both weights and noticed that the weights $\mathbf{W}_{ij} = |\mathbf{S}_{ij}| + |\mathbf{S}_{ji}|$ always yielded more accurate results for SMC; we thus used them then even though they can give an advantage over GCT, which uses exponential weights. Overall, the weight $\mathbf{W}_{ij} = |\mathbf{S}_{ij}| + |\mathbf{S}_{ji}|$ was used in the synthetic datasets II-VI of Section 4.1. The exponential weight was used in the rest of the experiments, that is, in synthetic dataset I and in the real or stylized applications. It was also used for dataset VI in Figure 6 under noise levels mostly higher than the 0.025 noise level used in Section 4.1. The collapse phenomenon is evident in Figure 6 for noise levels above 0.05.

The SCR algorithm has only one parameter σ_d which is set to 1 (similarly to the analogous parameter of GCT). EKM has no input parameters.

B Computation of Logarithm Maps and Distances

We discuss the complexity of computing logarithm maps for Grassmannians, symmetric PD matrices and spheres. We remark though that it is possible to compute the logarithm maps for data sampled from more general Riemannian manifolds and without knowledge of the manifold, but at a significantly slower rate (Mémoli and Sapiro, 2005). We also show that once the logarithm map is computed, then in all these cases the computation of the geodesic distances is of lower or equal order.

A fast way to compute the logarithm map of the Grassmannian $G(p, \ell)$ (whose dimension is $D = \ell(p - \ell)$) is provided in Gallivan et al. (2003). It requires a $p \times \ell$ matrix L , with orthogonal columns, and a $p \times p$ orthonormal matrix R for each subspace, where the subspace is spanned by the columns of L , with L comprising the first k columns of R . Given two pairs (L_1, R_1) and (L_2, R_2) for two subspaces, one needs to compute $\log_{L_1}(L_2)$. This computation, which is clarified in Gallivan et al. (2003), includes the singular value decomposition of $L_1^T L_2$ and $R_1^T L_2$. In total, the complexity is $\mathcal{O}(p^2 \ell)$, or equivalently, $\mathcal{O}((D/\ell + \ell)^2 \ell)$ (since $D = \ell(p - \ell)$).

For the set of $p \times p$ symmetric PD matrices (whose dimension is $D = p(p + 1)/2$), Ho et al. (2013b) computes the logarithm $\log_{M_1}(M_2)$ of any such matrices M_1 and M_2 by first finding the Cholesky decomposition $M_1 = GG^T$ and then computing $\log_{M_1}(M_2) = G \log(GM_2G)G$, where the latter log is the matrix logarithm. The complexities of all major operations (i.e., Cholesky decomposition, the matrix log-

arithm and the matrix multiplication) are $\mathcal{O}(p^3)$. Therefore, the total complexity is also of order $\mathcal{O}(p^3)$, or equivalently, $\mathcal{O}(D^{1.5})$ (since the dimension of the set of symmetric PD matrices is $D = p(p + 1)/2$).

The formula for finding the logarithm map on \mathbb{S}^D is (see Cetingul et al. (2014))

$$\log_{x_i}(x_j) = \frac{x_j - (x_i^T x_j)x_i}{\sqrt{1 - (x_i^T x_j)^2}} \cos^{-1}(x_i^T x_j),$$

where $x_i^T x_j$ is the (Euclidean) dot-vector product. Since it involves inner products and basic operations (also coordinatewise), it takes $\mathcal{O}(D)$ operations to compute it.

For $x_1, x_2 \in M$, $\text{dist}_g(x_1, x_2) = \|\log_{x_1}(x_2)\|_2$. Once we have the image $\log_{x_1}(x_2)$ (which is a vector in the tangent space), the Riemannian distance is computed as the Euclidean norm of the image vector, which involves a computation of order $\mathcal{O}(D)$. Since the algorithm already computes the logarithm maps, the additional cost for computing the geodesic distances are of lower order than the logarithm maps in all 3 cases.

C Computational complexity of GCT and TGCT

The computational complexity of GCT is examined per data-point x_i . It involves the computation of Riemannian distances and the logarithm map, which depends on the Riemannian manifold M (see estimates in Section B). The complexity of computing the Riemannian distance between x_i and x_j and the logarithm map for x_j w.r.t. x_i are denoted by CR and CL respectively (their computational complexity for the cases of the sphere, Grassmannian and PD matrices were discussed in Appendix B). A major part of GCT occurs in the r -neighborhood of x_i (WLOG), where r was defined as the average distance to the 30th nearest point from the associated data-point. To facilitate the analysis of computational complexity, we use instead of r the parameter k of k -nearest-neighbors (k -NN) around x_i . Due to the choice of r , we assume that $k \sim 30$.

The complexity for computing the k -NN of x_i is $\mathcal{O}(N \cdot \text{CR} + k \log(N))$, where $\mathcal{O}(N \cdot \text{CR})$ refers to the complexity of computing $N - 1$ distances, and $\mathcal{O}(k \log(N))$ refers to the effort of identifying the k smallest ones. The second step of Algorithm 2 is to solve the sparse optimization task in (3). Notice that due to $\|\cdot\|_2$, only the inner products of data-points are necessary to form the loss function in (3), which entails a complexity of order $\mathcal{O}(D)$. Given that only k -NN are involved in (3) and that their inner products are required to form the loss, (3) is a small scale convex optimization task that can be solved efficiently by any off-the-shelf solver such as the popular alternating direction method of multipliers (Glowinski and Marrocco, 1975; Gabay and Mercier, 1976) or the Douglas-Rachford algorithm (Bauschke and Combettes, 2011). The third step of Algorithm 2 is to find the top eigenvectors of the sample covariance matrix defined by the k neighbors of x_i . As shown in Section C.1 below the complexity of this step is $\mathcal{O}(D + k^3)$. Finally, to compute geodesic angles, $\mathcal{O}(N \cdot \text{CL} + ND)$ operations are necessary. Considering all N data-points, the total complexity for the main loop of GCT is $\mathcal{O}(N^2(\text{CR} + \text{CL} + D) + kN \log(N) + ND + Nk^3)$. After the main loop, spectral clustering is invoked on the $N \times N$ affinity matrix \mathbf{W} . The main computational burden is to identify K eigenvectors of an $N \times N$ matrix, which entails complexity of order $\mathcal{O}(KN^2)$ (K is the number of clusters). In summary, the complexity of GCT is $\mathcal{O}(N^2(\text{CR} + \text{CL} + D + K) + kN \log(N) + ND + Nk^3)$.

Note that in TGCT, the weights of non-neighboring points are set equal to zero, and geodesic angles are computed only for neighboring points, reducing thus the complexity of this step to $\mathcal{O}(N)$. Moreover, the affinity matrix is sparse in TGCT, effecting thus a potential decrease in the complexity of spectral clustering to the order of $\mathcal{O}(N \log N)$ (Knyazev, 2001; Kushnir et al., 2010). Therefore, TGCT's complexity becomes $\mathcal{O}(N^2 \text{CR} + (k + 1)N \log(N) + kN(\text{CL} + D) + Nk^3)$. The only step that contributes to N^2 in TGCT comes from k -NN. This complexity can be reduced by approximate nearest search. For example, for both the Sphere and the Grassmannian, Wang et al. (2013) established an $\mathcal{O}(N^\rho)$ algorithm for approximate nearest neighbor search, where $\rho > 0$ is a sufficiently small parameter. Therefore the total complexity of TGCT

for these special cases can be of order $\mathcal{O}(N^{1+\rho}\text{CR} + (k+1)N \log(N) + kN(\text{CL} + D) + Nk^3)$ (this includes also the preprocessing for the approximate nearest neighbors algorithm).

C.1 An Algebraic Trick for Fast Computation of the Tangent Subspace

Consider the $D \times k$ data matrix \mathbf{X} at a specific neighborhood with k points. We need to identify a few principal eigenvectors of the $D \times D$ covariance matrix $\mathbf{X}\mathbf{X}^T$. One can avoid such a costly direct computation (when D is large) by leveraging the following elementary facts from linear algebra: (i) If (λ, \mathbf{v}) is an eigenvalue-eigenvector pair of $\mathbf{X}^T\mathbf{X}$, then $(\lambda, \mathbf{X}\mathbf{v})$ is an eigenvalue-eigenvector pair of $\mathbf{X}\mathbf{X}^T$, and (ii) $\text{rank}(\mathbf{X}^T\mathbf{X}) = \text{rank}(\mathbf{X}\mathbf{X}^T)$. These facts suggest that the spectra of $\mathbf{X}^T\mathbf{X}$ and $\mathbf{X}\mathbf{X}^T$ coincide, and thus it is sufficient to compute the eigendecomposition of the much smaller $k \times k$ matrix $\mathbf{X}^T\mathbf{X}$, with complexity $\mathcal{O}(k^3)$, which renders the overall cost of eigendecomposition equal to $\mathcal{O}(D + k^3)$, including, for example, the cost of computing $\mathbf{X}\mathbf{v}$.

D Supplementary Details for the Proof of Theorem 1

D.1 Proof of Lemma 7

Suppose on the contrary that such a constant does not exist. Then there is a sequence $\{x_n\}_{n=1}^\infty \subset S_1 \cup S_2$ such that

$$\text{dist}_g(x_n, S_1 \cap S_2) \geq n \max\{\text{dist}_g(x, S_1), \text{dist}_g(x, S_2)\}. \quad (63)$$

By picking a subsequence if necessary, assume WLOG that $\{x_n\}_{n=1}^\infty \subset S_1$. Since S_1 is compact, there is always a convergent subsequence. Therefore, one may assume that $\{x_n\}_{n=1}^\infty \subset S_1$ is also convergent. We show that it converges to a point $z \in S_1 \cap S_2$.

Since $S_1 \cup S_2$ and $S_1 \cap S_2$ are compact, $\text{dist}_g(x_n, S_1 \cap S_2)$ is bounded. Equation (63) implies that $\text{dist}_g(x_n, S_2) \rightarrow 0$ as n approaches infinity. Suppose $\{x_n\}_{n=1}^\infty$ converges to a point $y \notin S_1 \cap S_2$. Then $\text{dist}_g(x_n, S_2) \rightarrow \text{dist}_g(y, S_2) > 0$ since $y \notin S_2$. This is a contradiction.

Now that $\{x_n\}_{n=1}^\infty$ converges to $z \in S_1 \cap S_2$, one may assume $\{x_n\}_{n=1}^\infty$ is in the normal coordinate chart Φ_z of $B(z, r)$ for some fixed $r > 0$. Denote $\mathbf{y}_n = \Phi_z^{-1}(x_n)$, $L_1 = \Phi_z^{-1}(S_1)$ and $L_2 = \Phi_z^{-1}(S_2)$. Since both S_1 and S_2 are geodesic submanifolds, L_1 and L_2 are two subspaces in $T_z M$. The sequence $\{\mathbf{y}_n\}_{n=1}^\infty \subset L_1$ approaches the origin. Lemma 17 of Arias-Castro et al. (2013) states that

$$\text{dist}_E(\mathbf{y}_n, L_1 \cap L_2) \leq \frac{\text{dist}_E(\mathbf{y}_n, L_2)}{\sin \theta_{\min}(L_1, L_2)},$$

where $\theta_{\min}(L_1, L_2)$ is the minimal nonzero principal angle between L_1 and L_2 . Let H be a subset of $B_z(\mathbf{0}, r)$ and arbitrarily fix a point $\mathbf{u} \in H$. It follows from (54) (applied with $R = \mathcal{O}(r)$) that

$$\text{dist}_E(\mathbf{y}_n, \mathbf{u})(1 - \mathcal{O}(r^2)) < \text{dist}_g(\mathbf{y}_n, \mathbf{u}) < \text{dist}_E(\mathbf{y}_n, \mathbf{u})(1 + \mathcal{O}(r^2)).$$

Since the term $\mathcal{O}(r^2)$ depends only on the metric g , not on \mathbf{y}_n or \mathbf{u} , it is easy to see that

$$\text{dist}_E(\mathbf{y}_n, H)(1 - \mathcal{O}(r^2)) < \text{dist}_g(\mathbf{y}_n, H) < \text{dist}_E(\mathbf{y}_n, H)(1 + \mathcal{O}(r^2)). \quad (64)$$

If we let $H = L_1 \cap L_2$ then (64) implies that

$$\text{dist}_g(\mathbf{y}_n, L_1 \cap L_2) \leq \frac{(1 + \mathcal{O}(r^2)) \text{dist}_g(\mathbf{y}_n, L_2)}{(1 - \mathcal{O}(r^2)) \sin \theta_{\min}(L_1, L_2)}.$$

This is equivalent to

$$\text{dist}_g(x_n, S_1 \cap S_2) \leq \frac{(1 + \mathcal{O}(r^2)) \text{dist}_g(x_n, S_2)}{(1 - \mathcal{O}(r^2)) \sin \theta_{\min}(L_1, L_2)} < \frac{2}{\sin \theta_0} \text{dist}_g(x_n, S_2)$$

for a fixed small r . This contradicts (63).

D.2 Proof of (38)

The measures μ_{x_0} and μ_z are used to denote the induced measures on $\Phi_{x_0}^{-1}(B(x_0, r) \cap (S_1 \cup S_2))$ and $\Phi_z^{-1}(B(x_0, r) \cap (S_1 \cup S_2))$ by $\mu_{gS_1} + \mu_{gS_2}$. Let $H = \Phi_{x_0}^{-1}(B(x_0, r) \cap (S_1 \cup S_2))$ and $\phi_{x_0} = \Phi_z^{-1} \circ \Phi_{x_0}$ be the transition map. Note that

$$\begin{aligned} \mathbb{E}_{\mu_{gS}} \mathbf{C}_{x_0}^z &= \mathbb{E}_{\mu_z} ((\mathbf{y} - \mathbb{E}_{\mu_z} \mathbf{y}) \cdot (\mathbf{y} - \mathbb{E}_{\mu_z} \mathbf{y})^T) \\ &= \frac{1}{\mu_z(\phi_{x_0}(H))^3} \int_{\mathbf{y} \in \phi_{x_0}(H)} \left(\int_{\mathbf{u} \in \phi_{x_0}(H)} (\mathbf{y} - \mathbf{u}) \mu_z(d\mathbf{u}) \cdot \int_{\mathbf{u} \in \phi_{x_0}(H)} (\mathbf{y} - \mathbf{u})^T \mu_z(d\mathbf{u}) \right) \mu_z(d\mathbf{y}). \end{aligned} \quad (65)$$

Let $\mathbf{y} = \phi_{x_0}(\mathbf{x})$ and $\mathbf{u} = \phi_{x_0}(\mathbf{v})$. We note that $\mathbf{x}, \mathbf{v} \in B(\mathbf{0}, r)$ and $\mathbf{y}, \mathbf{u} \in B(\mathbf{0}, (C' + 1)r)$. It follows from the triangle inequality, double application of (54) (first with $R = (C' + 1)r$ and next with $R = r$), the elementary bound $\text{dist}_E(\mathbf{r}, \mathbf{s}) \leq 2\text{diam}(M)$, where \mathbf{r}, \mathbf{s} are images by the logarithm map of points in M and $\text{diam}(M)$ is the diameter of M and the identity $l_g(\mathbf{y}, \mathbf{u}) = l_g(\mathbf{x}, \mathbf{v})$ (which holds since ϕ_{x_0} preserves the Riemannian distance) that

$$\begin{aligned} |||\mathbf{y} - \mathbf{u}||_2 - \|\mathbf{x} - \mathbf{v}\|_2| &= |||\mathbf{y} - \mathbf{u}||_2 - l_g(\mathbf{y}, \mathbf{u}) + l_g(\mathbf{y}, \mathbf{u}) - \|\mathbf{x} - \mathbf{v}\|_2| \\ &\leq |||\mathbf{y} - \mathbf{u}||_2 - l_g(\mathbf{y}, \mathbf{u})| + |l_g(\mathbf{x}, \mathbf{v}) - \|\mathbf{x} - \mathbf{v}\|_2| \leq 2C_4 \text{diam}(M) [(C' + 1)^2 + 1] r^2. \end{aligned} \quad (66)$$

Applying Taylor's expansion to $\mathbf{y} = \phi_{x_0}(\mathbf{x})$, and using the fact that $\|\mathbf{x}\|_2 \leq r$, we note that

$$\|\mathbf{y} - \mathbf{b}_{x_0} - \mathbf{A}_{x_0} \mathbf{x}\|_2 \leq C_S'' r^2, \quad (67)$$

where \mathbf{b}_{x_0} and \mathbf{A}_{x_0} depend only on x_0 and C_S'' is a constant depending on the Riemannian metric g . Applying the triangle inequality, (66) and (67) (first with $\mathbf{y} = \phi_{x_0}(\mathbf{x})$ and next with $\mathbf{u} = \phi_{x_0}(\mathbf{v})$ instead of \mathbf{y}) we conclude that for all $\mathbf{x}, \mathbf{v} \in B_{x_0}(\mathbf{0}, r)$

$$\begin{aligned} &|||\mathbf{A}_{x_0}(\mathbf{x} - \mathbf{v})||_2 - \|\mathbf{x} - \mathbf{v}\|_2| \\ &\leq |||\mathbf{y} - \mathbf{u}||_2 - \|\mathbf{x} - \mathbf{v}\|_2| + \|\mathbf{y} - \mathbf{b}_{x_0} - \mathbf{A}_{x_0} \mathbf{x}\|_2 + \|\mathbf{u} - \mathbf{b}_{x_0} - \mathbf{A}_{x_0} \mathbf{v}\|_2 \\ &\leq [2C_4 \text{diam}(M) ((C' + 1)^2 + 1) + 2C_S''] r^2. \end{aligned} \quad (68)$$

In particular, suppose $\|\mathbf{x} - \mathbf{v}\|_2 = r$, then (68) implies that for any unit-length vectors $\mathbf{w} \in \mathbb{R}^D$ (\mathbb{R}^D is identified with T_{x_0})

$$|||\mathbf{A}_{x_0} \mathbf{w}||_2 - 1| \leq [2C_4 \text{diam}(M) ((C' + 1)^2 + 1) + 2C_S''] r. \quad (69)$$

We prove below in Appendix D.2.1 that there exists an orthogonal matrix \mathbf{R}_{x_0} such that

$$\mathbf{A}_{x_0} = \mathbf{R}_{x_0} + \mathcal{O}(r). \quad (70)$$

This leads to

$$\mathbf{y} = \mathbf{b}_{x_0} + \mathbf{R}_{x_0} \mathbf{x} + \mathcal{O}(r^2) \quad \text{and} \quad \mathbf{u} = \mathbf{b}_{x_0} + \mathbf{R}_{x_0} \mathbf{v} + \mathcal{O}(r^2).$$

Consequently,

$$\mathbf{y} - \mathbf{u} = \mathbf{R}_{x_0}(\mathbf{x} - \mathbf{v}) + \mathcal{O}(r^2). \quad (71)$$

We also note that since μ_z and μ_{x_0} are induced from μ , then

$$\mu_z(\phi_{x_0}(H)) = \mu_{x_0}(H) \quad (72)$$

At last, (38) is concluded by applying (65) (first with \mathbf{y} and \mathbf{u} and next with \mathbf{x} and \mathbf{v} while using appropriate change of variables), (71) and (72).

D.2.1 Proof of (70)

We show that if \mathbf{A} is an $D \times D$ matrix such that $|\|\mathbf{A}\mathbf{w}\|_2 - 1| \leq Cr$ for all unit-length vectors $\mathbf{w} \in \mathbb{R}^D$ and a fixed constant $C > 0$, then there exists an orthogonal matrix \mathbf{R} such that $\mathbf{A} = \mathbf{R} + \mathcal{O}(r)$. In other words, the ij th entries of \mathbf{A} and \mathbf{R} satisfy

$$|\mathbf{A}_{ij} - \mathbf{R}_{ij}| \leq f(C, D)r \quad (73)$$

for a bounded function f (we only show below that the RHS of (73) is bounded by a constant times r , but it is not hard to see that this constant depends on C and D ; this dependence is used later in (97) in order to provide a clearer idea of the constant C'_S).

By performing Gram-Schmidt orthogonalization on rows, the matrix \mathbf{A} can be written as a product of an upper triangular matrix \mathbf{U} and an orthogonal matrix \mathbf{R} (this is the \mathbf{RQ} decomposition of \mathbf{A} , but with \mathbf{U} and \mathbf{R} used instead of \mathbf{R} and \mathbf{Q} respectively). Since \mathbf{R} preserves the length of vectors, the condition on \mathbf{A} becomes

$$|\|\mathbf{U}\mathbf{w}\|_2 - 1| \leq Cr, \quad (74)$$

for all unit-length vectors \mathbf{w} . It is enough to show that up to a change of sign of the rows of \mathbf{R} : $\mathbf{U} = \mathbf{I} + \mathcal{O}(r)$. This is proved by induction on D .

If $D = 1$, then \mathbf{U} is a 1×1 matrix. Let $\mathbf{w} = 1$. In this case (74) implies that $\mathbf{U} = \pm 1 + \mathcal{O}(r)$. By possible change of sign of \mathbf{R} we conclude that $\mathbf{U} = 1 + \mathcal{O}(r)$.

We assume that the claim is true for $D = k - 1$. Let \mathbf{U} be a $k \times k$ upper rectangular matrix and express it as follows:

$$\mathbf{U} = \begin{pmatrix} \mathbf{V}_{k-1 \times k-1} & \mathbf{x}_{k-1 \times 1} \\ \mathbf{0}_{1 \times k-1} & \mathbf{U}_{kk} \end{pmatrix},$$

where \mathbf{V} is $(k - 1) \times (k - 1)$ upper triangular matrix, $\mathbf{0}_{1 \times k-1}$ is a row vector of $k - 1$ zeros, $\mathbf{x}_{k-1 \times 1}$ is a column vector in \mathbb{R}^{k-1} and $\mathbf{U}_{kk} \in \mathbb{R}$. We assume that \mathbf{U} satisfies (74) and show that $\mathbf{U} = \mathbf{I} + \mathcal{O}(r)$ by basic estimates with different choices of $\mathbf{w} \in \mathbb{R}^k$ used in (74).

Assume first that $\mathbf{w} = [\mathbf{v}^T, 0]^T$, where $\mathbf{v} \in \mathbb{R}^{k-1}$ is of unit-length. Then (74) implies that

$$|\|\mathbf{V}\mathbf{v}\|_2 - 1| \leq Cr. \quad (75)$$

The induction hypothesis and (75) results in the estimate

$$\mathbf{V} = \mathbf{I} + \mathcal{O}(r) \quad (76)$$

up to a change of sign in the first $k - 1$ rows of \mathbf{R} (the rotation associated with \mathbf{U}).

Next, we show that $\mathbf{U}_{kk} = 1 + \mathcal{O}(r)$. We first let $\mathbf{w} = [\mathbf{0}_{1 \times k-1}, 1]^T$; in this case (74) implies that

$$\sqrt{\|\mathbf{x}\|_2^2 + \mathbf{U}_{kk}^2} - 1 = \mathcal{O}(r), \quad (77)$$

which leads to

$$\|\mathbf{x}\|_2^2, |\mathbf{U}_{kk}|^2 \leq 1 + \mathcal{O}(r). \quad (78)$$

We next let $\mathbf{w} = [-\mathbf{x}^T, 1]^T / \|[-\mathbf{x}^T, 1]^T\|_2$. Then (74), with $\|\mathbf{x}\|_2^2$ being bounded by $1 + \mathcal{O}(r)$, implies that

$$\sqrt{\mathbf{U}_{kk}^2 + \mathcal{O}(r^2)} - \|[-\mathbf{x}^T, 1]^T\|_2 = \mathcal{O}(r). \quad (79)$$

Moving the second term of the LHS of (79) to the RHS of (79) and squaring both sides result in

$$\mathbf{U}_{kk}^2 \geq \|[-\mathbf{x}^T, 1]^T\|_2^2 - \mathcal{O}(r) \geq 1 - \mathcal{O}(r). \quad (80)$$

The combination of (78) and (80) implies that

$$|\mathbf{U}_{kk}^2 - 1| \leq \mathcal{O}(r). \quad (81)$$

Since $\mathbf{U}_{kk} \geq 0$ WLOG (otherwise one can change the sign of the k th row of \mathbf{R}) and since $|\mathbf{U}_{kk}^2 - 1|$ is a Lipschitz function on \mathbf{U}_{kk} , (81) implies that

$$|\mathbf{U}_{kk} - 1| \leq \mathcal{O}(r). \quad (82)$$

In other words, $\mathbf{U}_{kk} = 1 + \mathcal{O}(r)$.

At last, we show that $\mathbf{x}_i = \mathcal{O}(r)$. Moving the second term of the LHS of (77) to the RHS of (77) and squaring both sides result in

$$\|x\|_2^2 + \mathbf{U}_{kk}^2 = 1 + \mathcal{O}(r). \quad (83)$$

It follows from (82) and (83) that $\|\mathbf{x}\|_2^2 = \mathcal{O}(r)$, which implies that

$$\mathbf{x}_i = \mathcal{O}(\sqrt{r}). \quad (84)$$

Denote the standard basis of \mathbb{R}^k by $\{\mathbf{e}_i\}_{i=1}^k$, that is, $\mathbf{e}_1 = [1, 0, \dots, 0]^T, \dots, \mathbf{e}_k = [0, \dots, 0, 1]^T$. Let $\mathbf{w}_i = \frac{\sqrt{2}}{2}\mathbf{e}_i + \frac{\sqrt{2}}{2}\mathbf{e}_k$. Plugging \mathbf{w}_i into (74) and further simplification result in

$$\left[\frac{1}{2}(\mathbf{x}_1^2 + \dots + \mathbf{x}_{k-1}^2) + 1 + \frac{1}{2}\mathbf{x}_i + \mathcal{O}(r) \right]^{1/2} = 1 + \mathcal{O}(r). \quad (85)$$

Further application of (84) into (85) yields the equality

$$\left[1 + \frac{1}{2}\mathbf{x}_i + \mathcal{O}(r) \right]^{1/2} = 1 + \mathcal{O}(r). \quad (86)$$

Finally, squaring both sides of (86) and simplifying concludes the desired estimate

$$\mathbf{x}_i = \mathcal{O}(r). \quad (87)$$

Equations (76), (82) and (87) imply that $\mathbf{U} = \mathbf{I} + \mathcal{O}(r)$ (up to a change of signs of the rows of \mathbf{R}) and thus conclude the induction and consequently (70).

D.3 Proof of (39)

Let $H_1 = B_I(\Phi_z^{-1}(x_0), r - \mathcal{O}(r^2)) \cap \Phi_z^{-1}(S_1 \cup S_2)$ and $H_2 = B_I(\Phi_z^{-1}(x_0), r + \mathcal{O}(r^2)) \cap \Phi_z^{-1}(S_1 \cup S_2)$. It follows from (54) (applied with $R = \mathcal{O}(r)$) that

$$B_I(\Phi_z^{-1}(x_0), r - \mathcal{O}(r^2)) \subset \Phi_z^{-1}(B(x_0, r)) \subset B_I(\Phi_z^{-1}(x_0), r + \mathcal{O}(r^2)). \quad (88)$$

The intersection of all sets in (88) with $L_1 \cup L_2 = \Phi_z^{-1}(S_1 \cup S_2)$ and the definitions of H_1, H_2 and H' result in the set inequality

$$H_1 \subset H' \subset H_2. \quad (89)$$

Thus,

$$H \setminus H' \subset H_2 \setminus H', \quad H' \setminus H \subset H' \setminus H_1. \quad (90)$$

By first applying (90) (or its consequence $(H_2 \setminus H') \cup (H' \setminus H_1) = H_2 \setminus H_1$) and then direct estimates (whose details are excluded) we obtain that

$$\mu_{ES}((H_2 \setminus H') \cup (H' \setminus H_1)) = \mu_{ES}(H_2 \setminus H_1) = \mathcal{O}(r)\mu_{ES}(H_1). \quad (91)$$

Finally, (39) follows from (90) and (91).

D.4 Proof of (54)

Denote by $l(t)$ the parameterized line segment in $T_{x_1}M$ connecting $l(0) = \mathbf{x}$ and $l(1) = \mathbf{y}$, where \mathbf{x} and \mathbf{y} are specified in (54). We note that

$$\begin{aligned} \text{dist}_g(\mathbf{x}, \mathbf{y}) &= \int_0^1 \sqrt{l'(t)^T g(l(t)) l'(t)} dt = \int_0^1 \sqrt{l'(t)^T (I + \mathcal{O}(R^2)) l'(t)} dt \\ &= \text{dist}_E(\mathbf{x}, \mathbf{y}) + \mathcal{O}(R^2) \text{dist}_E(\mathbf{x}, \mathbf{y}). \end{aligned} \quad (92)$$

Equation (92) clearly implies (54), where $C_4 > 0$ depends only on the Riemannian manifold M .

D.5 Proof of (58)

We first claim that for any $\alpha > 0$

$$\sin(\theta_{\max}(T_{x_1}^E S_1, T_{x_1} S_1)) \leq \|\mathbf{P}_{T_{x_1}^E S_1} - \mathbf{P}_{T_{x_1} S_1}\| < \frac{\sqrt{2} \|\mathbf{C}_{x_1} - \frac{\alpha r^2}{d+2} \mathbf{P}_{T_{x_1} S_1}\|}{\frac{\alpha r^2}{d+2}}. \quad (93)$$

The first inequality of (93) follows from Lemma 15 in Arias-Castro et al. (2013). Whereas the second inequality follows from the Davis-Kahan Theorem (Davis and Kahan, 1970).

For the rest of the proof we upper bound the RHS of (93). We work in the tangent space $T_z M$, where z is defined as

$$z = \operatorname{argmin}_{y \in S_1 \cap S_2} \text{dist}_g(x_1, y).$$

Similarly as in the proof of Proposition 8, if argmin is not uniquely defined, z is arbitrarily chosen among all minimizers. Let the composition map $\phi_{x_1} = \Phi_z^{-1} \circ \Phi_{x_1}$ be the transition map from $T_{x_1}M$ to $T_z M$. Note that ϕ_{x_1} maps the subspace $T_{x_1} S_1$ to another subspace $T_z S_1$. Let $\mathbf{R}_{x_1}(L_1)$ denote the image of L_1 in $T_z M$ under the rotation matrix \mathbf{R}_{x_1} (here we identify both $T_{x_1}M$ and $T_z M$ with \mathbb{R}^D via their normal coordinate charts). Using the new terminology the main term in the RHS of (93) can be expressed as follows

$$\|\mathbf{C}_{x_1} - \frac{\alpha r^2}{d+2} \mathbf{P}_{T_{x_1} S_1}\| = \|\mathbf{R}_{x_1} \mathbf{C}_{x_1} \mathbf{R}_{x_1}^T - \frac{\alpha r^2}{d+2} \mathbf{P}_{\mathbf{R}_{x_1}(T_{x_1} S_1)}\|. \quad (94)$$

The RHS of (94) can be bounded by the triangle inequality and (41) as follows

$$\begin{aligned} &\|\mathbf{R}_{x_1} \mathbf{C}_{x_1} \mathbf{R}_{x_1}^T - \frac{\alpha r^2}{d+2} \mathbf{P}_{\mathbf{R}_{x_1}(T_{x_1} S_1)}\| \leq \|\mathbf{R}_{x_1} \mathbf{C}_{x_1} \mathbf{R}_{x_1}^T - \mathbb{E}_{\mu_{ES}} \mathbf{C}_{H'}\| \\ &+ \|\mathbb{E}_{\mu_{ES}} \mathbf{C}_{H'} - \frac{\alpha r^2}{d+2} \mathbf{P}_{T_z S_1}\| + \|\frac{\alpha r^2}{d+2} \mathbf{P}_{T_z S_1} - \frac{\alpha r^2}{d+2} \mathbf{P}_{\mathbf{R}_{x_1}(T_{x_1} S_1)}\| \\ &\leq C'_S r^3 + \|\mathbb{E}_{\mu_{ES}} \mathbf{C}_{H'} - \frac{\alpha r^2}{d+2} \mathbf{P}_{T_z S_1}\| + \|\frac{\alpha r^2}{d+2} \mathbf{P}_{T_z S_1} - \frac{\alpha r^2}{d+2} \mathbf{P}_{\mathbf{R}_{x_1}(T_{x_1} S_1)}\|. \end{aligned} \quad (95)$$

Next, we bound the last term in the RHS of (95). It follows from (69), (67), (73) (which implies (70)) that for $\mathbf{y} = \phi_{x_1}(\mathbf{x})$

$$\|\mathbf{y} - \mathbf{b}_{x_1} - \mathbf{R}_{x_1} \mathbf{x}\|_2 \leq C_S''' r^2 \quad \forall \|\mathbf{x}\|_2 \leq r, \quad (96)$$

where

$$C_S''' = D \cdot f(2C_4 \text{diam}(M)((C' + 1)^2 + 1) + 2C_S'', D) + C_S''. \quad (97)$$

It is immediate to see that $\mathbf{b} \in T_z S_1$ by letting $\mathbf{x} = \mathbf{0}$ in the Taylor's expansion. If $\mathbf{v} \in \mathbf{R}_{x_1}(T_{x_1} S_1)$ is a vector such that $\|\mathbf{v}\|_2 = r$ and $\theta(\mathbf{v}, T_z S_1) = \theta_{\max}(\mathbf{R}_{x_1}(T_{x_1} S_1), T_z S_1)$, then (96) and the fact that $\phi_{x_1}(\mathbf{R}_{x_1}^{-1} \mathbf{v}) - \mathbf{b} \in T_z S_1$ imply that $\text{dist}(\mathbf{v}, T_z S_1) \leq C_S''' r^2$. Consequently,

$$\|\mathbf{P}_{\mathbf{R}_{x_1}(T_{x_1} S_1)} - \mathbf{P}_{T_z S_1}\| = \sin(\theta_{\max}(\mathbf{R}_{x_1}(T_{x_1} S_1), T_z S_1)) = \frac{\text{dist}(\mathbf{v}, T_z S_1)}{\|\mathbf{v}\|_2} \leq C_S''' r. \quad (98)$$

If $\alpha_0 = (1 + (1 - \delta^2(x_1))_+^{d/2})^{-1}$ (the same as in Lemma 21 of Arias-Castro et al. (2013)), then the argument in Arias-Castro et al. (2013, page 41) shows that

$$\|\mathbb{E}_{\mu_{ES}} \mathbf{C}_{H'} - \frac{\alpha_0 r^2}{d+2} \mathbf{P}_{T_z S_1}\| \leq 2C_2^{\frac{d}{2}} \eta^{\frac{d}{d+2}} r^2. \quad (99)$$

Inequalities (95) (with $\alpha = \alpha_0$), (98) (with $\alpha = \alpha_0$) and (99) imply that

$$\|\mathbf{R}_{x_1} \mathbf{C}_{x_1} \mathbf{R}_{x_1}^T - \frac{\alpha_0 r^2}{d+2} \mathbf{P}_{\mathbf{R}_{x_1}(T_{x_1} S_1)}\| \leq C'_S r^3 + 2C_2^{\frac{d}{2}} \eta^{\frac{d}{d+2}} r^2 + \frac{C'''_S \alpha_0}{d+2} r^3. \quad (100)$$

Plugging (94) (with $\alpha = \alpha_0$) and (100) in (93) (with $\alpha = \alpha_0$) and applying the fact that $\frac{1}{2} \leq \alpha_0 \leq 1$ yield

$$\sin(\theta_{\max}(T_{x_1}^E S_1, T_{x_1} S_1)) < 2\sqrt{2}(d+2)(C'_S r + 2C_2^{\frac{d}{2}} \eta^{\frac{d}{d+2}} + \frac{C'''_S}{d+2} r). \quad (101)$$

Let

$$C'_3 = 2\sqrt{2}(d+2) \max(2C_2^{\frac{d}{2}}, C'_S + \frac{C'''_S}{d+2}), \quad (102)$$

then (58) clearly follows from (101) and (102).

D.6 Proof of (59)

We prove(59), while generalizing the setting to work with two subspaces L_1, L_2 and a line l . Let $\angle(l, L_1) = \theta_1$ and $\angle(l, L_2) = \theta_2$. Assume that

$$\theta_1 \leq \alpha \quad (103)$$

for an arbitrarily fixed $0 < \alpha < \pi/2$. We use the fact that $\sin(\theta)$ is a concave function. If $\theta_2 > \alpha$, then

$$\frac{1 - \sin(\alpha)}{\pi/2 - \alpha} \leq \frac{\sin(\theta_2) - \sin(\alpha)}{\theta_2 - \alpha} < \frac{\sin(\theta_2) - \sin(\theta_1)}{\theta_2 - \theta_1}. \quad (104)$$

On the other hand, the fact that $\sin^{-1}(x)$ is a Lipschitz function over the interval $[0, \sin(\alpha)]$ implies that if $\theta_2 \leq \alpha$,

$$|\theta_2 - \theta_1| \leq \frac{1}{\cos(\alpha)} |\sin(\theta_2) - \sin(\theta_1)| \quad \text{for } \theta_1, \theta_2 \in [0, \alpha]. \quad (105)$$

Equation (104) and (105) imply that

$$|\theta_2 - \theta_1| \leq \max\left(\frac{\pi/2 - \alpha}{1 - \sin(\alpha)}, \frac{1}{\cos(\alpha)}\right) |\sin(\theta_2) - \sin(\theta_1)|. \quad (106)$$

If $\alpha = \pi/6$, then (106) and Lemma 3.2 of Lerman and Zhang (2014) lead to the inequality

$$|\theta_2 - \theta_1| \leq \frac{2\pi\sqrt{d}}{3} \sin(\theta_{\max}(L_1, L_2)). \quad (107)$$

Thus,

$$\theta_1 \geq \theta_2 - \frac{2\pi\sqrt{d}}{3} \sin(\theta_{\max}(L_1, L_2)) \quad (108)$$

as long as (103) holds. If (103) is not assume, (108) can be replaced with

$$\theta_1 \geq \min(\theta_2 - \frac{2\pi\sqrt{d}}{3} \sin(\theta_{\max}(L_1, L_2)), \pi/6) \quad \forall \theta_1 \in [0, \pi/2], \quad (109)$$

which translates to (59).

References

- A. Aldroubi. A review of subspace segmentation: Problem, nonlinear approximations, and applications to motion segmentation. *ISRN Signal Processing*, 2013(Article ID 417492):1–13, 2013.
- E. Arias-Castro, G. Chen, and G. Lerman. Spectral clustering based on local linear approximations. *Electron. J. Statist.*, 5:1537–1587, 2011.
- E. Arias-Castro, G. Lerman, and T. Zhang. Spectral clustering based on local PCA. *ArXiv e-prints*, 2013.
- D. Barbará and P. Chen. Using the fractal dimension to cluster datasets. In *KDD*, pages 260–264, 2000.
- R. Basri, T. Hassner, and L. Zelnik-Manor. Approximate nearest subspace search. *IEEE Transactions on Pattern Analysis and Machine Intelligence*, 33(2):266–278, 2011.
- H. H. Bauschke and P. L. Combettes. *Convex Analysis and Monotone Operator Theory in Hilbert Spaces*. Springer, New York, 2011.
- T. E. Boult and L. G. Brown. Factorization-based segmentation of motions. In *Proceedings of the IEEE Workshop on Visual Motion*, pages 179–186, 1991.
- P. Bradley and O. Mangasarian. k-plane clustering. *J. Global optim.*, 16(1):23–32, 2000.
- E. J. Canales-Rodriguez, L. Melie-Garcia, Y. Iturria-Medina, and Y. Aleman-Gomez. Website, 2013. http://neuroimagen.es/webs/hardi_tools/.
- H. E. Cetingul and R. Vidal. Intrinsic mean shift for clustering on Stiefel and Grassmann manifolds. In *Proc. CVPR*, pages 1896–1902, June 2009.
- H. E. Cetingul, M. J. Wright, P. M. Thompson, and R. Vidal. Segmentation of high angular resolution diffusion MRI using sparse Riemannian manifold clustering. *IEEE Trans. Medical Imaging*, 33(2):301–317, Feb. 2014.
- G. Chen and G. Lerman. Spectral curvature clustering (SCC). *Int. J. Comput. Vision*, 81:317–330, 2009a.
- G. Chen and G. Lerman. Foundations of a multi-way spectral clustering framework for hybrid linear modeling. *Found. Comput. Math.*, 9(5):517–558, 2009b.
- J. Costeira and T. Kanade. A multibody factorization method for independently moving objects. *International Journal of Computer Vision*, 29(3):159–179, 1998.
- C. Davis and W. M. Kahan. The rotation of eigenvectors by a perturbation. III. *SIAM J. Numerical Analysis*, 7:1–46, Mar. 1970.
- M. P. do Carmo. *Riemannian Geometry*. Birkhäuser, Boston, 1992.
- G. Doretto, A. Chiuso, Y. N. Wu, and S. Soatto. Dynamic textures. *International J. Computer Vision*, 51(2):91–109, 2003.
- E. Elhamifar and R. Vidal. Sparse subspace clustering. In *Proc. CVPR*, 2009.
- E. Elhamifar and R. Vidal. Sparse manifold clustering and embedding. In *NIPS*, pages 55–63, 2011.
- E. Elhamifar and R. Vidal. Sparse subspace clustering: Algorithm, theory, and applications. *Pattern Analysis and Machine Intelligence, IEEE Transactions on*, PP(99):1–1, 2013. ISSN 0162-8828.

- D. Gabay and B. Mercier. A dual algorithm for the solution of nonlinear variational problems via finite-element approximations. *Comp. Math. Appl.*, 2:17–40, 1976.
- K. Gallivan, A. Srivastava, X. Liu, and P. V. Dooren. Efficient algorithms for inferences on Grassmann manifolds. In *Proc. SSP*, pages 315–318, 2003.
- B. Ghanem and N. Ahuja. Maximum margin distance learning for dynamic texture recognition. In *ECCV (2)*, pages 223–236, 2010.
- A. Gionis, A. Hinneburg, S. Papadimitriou, and P. Tsaparas. Dimension induced clustering. In *KDD*, pages 51–60, 2005.
- R. Glowinski and A. Marrocco. Sur l’approximation par éléments finis et la résolution par pénalisation-dualité d’une classe de problèmes de Dirichlet non linéaires. *Rev. Francaise d’Aut. Inf. Rech. Oper.*, 9(2):41–76, 1975.
- A. Goh and R. Vidal. Clustering and dimensionality reduction on Riemannian manifolds. In *Proc. CVPR*, pages 1–7, June 2008.
- A. Goldberg, X. Zhu, A. Singh, Z. Xu, and R. Nowak. Multi-manifold semi-supervised learning. In *Proc. CVPR*, volume 5, pages 169–176, 2009.
- D. Gong, X. Zhao, and G. Medioni. Robust multiple manifolds structure learning. In *Proc. ICML*, pages 321–328, 2012.
- A. Gray. Comparison theorems for the volumes of tubes as generalizations of the weyl tube formula. *Topology*, 21(2):201 – 228, 1982.
- P. Gruber and F. J. Theis. Grassmann clustering. In *Proc. EUSIPCO*, 2006.
- Q. Guo, H. Li, W. Chen, I-F. Shen, and J. Parkkinen. Manifold clustering via energy minimization. In *Proc. ICMLA*, pages 375–380, 2007.
- M. T. Harandi, C. Sanderson, C. Shen, and B. C. Lovell. Dictionary learning and sparse coding on Grassmann manifolds: An extrinsic solution. *Proc. ICCV*, 2013.
- G. Haro, G. Randall, and G. Sapiro. Stratification learning: Detecting mixed density and dimensionality in high dimensional point clouds. *Neural Information Processing Systems*, 2006.
- J. Ho, M. Yang, J. Lim, K. Lee, and D. Kriegman. Clustering appearances of objects under varying illumination conditions. In *Proceedings of International Conference on Computer Vision and Pattern Recognition*, volume 1, pages 11–18, 2003.
- J. Ho, Y. Xie, and B. Vemuri. On a nonlinear generalization of sparse coding and dictionary learning. In *Proc. ICML*, volume 28, pages 1480–1488, 2013a.
- J. Ho, Y. Xie, and B. C. Vemuri. On a nonlinear generalization of sparse coding and dictionary learning. In *Proceedings of the 30th International Conference on Machine Learning, ICML 2013, Atlanta, GA, USA, 16-21 June 2013*, pages 1480–1488, 2013b.
- K. Kanatani. Motion segmentation by subspace separation and model selection. In *Proc. of 8th ICCV*, volume 3, pages 586–591. Vancouver, Canada, 2001.
- K. Kanatani. Evaluation and selection of models for motion segmentation. In *7th ECCV*, volume 3, pages 335–349, May 2002.

- A. Knyazev. Toward the optimal preconditioned eigensolver: Locally optimal block preconditioned conjugate gradient method. *SIAM Journal on Scientific Computing*, 23(2):517–541, 2001.
- D. Kushnir, M. Galun, and A. Brandt. Fast multiscale clustering and manifold identification. *Pattern Recognition*, 39(10):1876–1891, 2006.
- D. Kushnir, M. Galun, and A. Brandt. Efficient multilevel eigensolvers with applications to data analysis tasks. *IEEE Trans. Pattern Anal. Mach. Intell.*, 32(8):1377–1391, 2010.
- G. Lerman and J. T. Whitehouse. On d -dimensional d -semimetrics and simplex-type inequalities for high-dimensional sine functions. *J. Approx. Theory*, 156(1):52–81, 2009.
- G. Lerman and T. Zhang. Robust recovery of multiple subspaces by geometric l_p minimization. *Annals of Statistics*, 39(5):2686–2715, 2011.
- G. Lerman and T. Zhang. l_p -recovery of the most significant subspace among multiple subspaces with outliers. *Constructive Approximation*, pages 1–57, 2014.
- G. Liu, Z. Lin, S. Yan, J. Sun, Y. Yu, and Y. Ma. Robust recovery of subspace structures by low-rank representation. *IEEE PAMI*, 35, 2013.
- Y. M. Lui. Advances in matrix manifolds for computer vision. *Image Vision Comput.*, 30(6-7):380–388, 2012.
- Y. Ma, H. Derksen, W. Hong, and J. Wright. Segmentation of multivariate mixed data via lossy coding and compression. *IEEE Transactions on Pattern Analysis and Machine Intelligence*, 29(9):1546–1562, September 2007.
- Y. Ma, A. Y. Yang, H. Derksen, and R. Fossum. Estimation of subspace arrangements with applications in modeling and segmenting mixed data. *SIAM Review*, 50(3):413–458, 2008.
- F. Mémoli and G. Sapiro. Distance functions and geodesics on submanifolds of \mathbb{R}^d and point clouds. *SIAM Journal of Applied Mathematics*, 65(4):1227–1260, 2005.
- A. Y. Ng, M. I. Jordan, and Y. Weiss. On spectral clustering: Analysis and an algorithm. In *NIPS*, pages 849–856, 2001.
- N. Nikvand. Website, 2013. <https://ece.uwaterloo.ca/~nnikvand/Coderep/spectralclustering-1.1/>.
- S. O’Hara, Y. M. Lui, and B. A. Draper. Unsupervised learning of human expressions, gestures, and actions. In *Proc. Automatic Face Gesture Recognition and Workshops*, pages 1–8, March 2011.
- N. Ozay, M. Sznaiar, C. Lagoa, and O. Camps. GPCA with denoising: A moments-based convex approach. In *Computer Vision and Pattern Recognition (CVPR), 2010 IEEE Conference on*, pages 3209–3216, 2010.
- B. Poling and G. Lerman. A new approach to two-view motion segmentation using global dimension minimization. *International Journal of Computer Vision*, 108(3):165–185, 2014.
- M. Polito and P. Perona. Grouping and dimensionality reduction by locally linear embedding. In *Advances in Neural Information Processing Systems (NIPS)*, volume 14, pages 1255–1262, 2001.
- I. U. Rahman, I. Drori, V. C. Stodden, D. L. Donoho, and P. Schröder. Multiscale representations for manifold-valued data. *Multiscale Model. Simul.*, 4(4):1201–1232 (electronic), 2005. ISSN 1540-3459.

- T. Randen. Website, 2014. <http://www.ux.uis.no/~tranden/brodatz.html>.
- Y. Rathi, A. Tannenbaum, and O. V. Michailovich. Segmenting images on the tensor manifold. In *CVPR*, 2007.
- M. Soltanolkotabi and E. J. Candès. A geometric analysis of subspace clustering with outliers. *Ann. Stat.*, 40(4):2195–2238, 2012.
- M. Soltanolkotabi, E. Elhamifar, and E. J. Candès. Robust subspace clustering. *Ann. Stat.*, 42(2):669–699, 2014.
- R. Souvenir and R. Pless. Manifold clustering. In *Proceedings of the 10th International Conference on Computer Vision (ICCV 2005)*, volume 1, pages 648–653, 2005.
- G. W. Stewart and J. G. Sun. *Matrix perturbation theory*. Computer Science and Scientific Computing. Academic Press Inc., Boston, MA, 1990. ISBN 0-12-670230-6.
- R. Subbarao and P. Meer. Nonlinear mean shift for clustering over analytic manifolds. In *Proc. CVPR*, volume 1, pages 1168–1175, June 2006.
- M. Tipping and C. Bishop. Mixtures of probabilistic principal component analysers. *Neural Computation*, 11(2):443–482, 1999.
- J. Y. Tou, Y. H. Tay, and P. Y. Lau. Gabor filters as feature images for covariance matrix on texture classification problem. In *Advances in Neuro-Information Processing*, volume 5507 of *Lecture Notes in Computer Science*, pages 745–751. Springer Berlin Heidelberg, 2009.
- P. Tseng. Nearest q -flat to m points. *Journal of Optimization Theory and Applications*, 105:249–252, 2000.
- P. Turaga, A. Veeraraghavan, A. Srivastava, and R. Chellappa. Statistical computations on Grassmann and Stiefel manifolds for image and video-based recognition. *IEEE PAMI*, 33(11):2273–2286, 2011.
- O. Tuzel, R. Subbarao, and P. Meer. Simultaneous multiple 3D motion estimation via mode finding on Lie groups. In *Proc. ICCV*, volume 1, pages 18–25, Oct. 2005.
- R. Vidal. Subspace clustering. *SPM*, 28:52–68, 2011.
- R. Vidal, Y. Ma, and S. Sastry. Generalized principal component analysis (GPCA). *IEEE Transactions on Pattern Analysis and Machine Intelligence*, 27(12), 2005.
- X. Wang, S. Atev, J. Wright, and G. Lerman. Fast subspace search via grassmannian based hashing. In *Computer Vision (ICCV), 2013 IEEE International Conference on*, pages 2776–2783, Dec 2013.
- Y. Wang and G. Mori. Human action recognition by semilattent topic models. *IEEE Trans. Pattern Anal. Mach. Intell.*, 31(10):1762–1774, 2009.
- Y. Wang, Y. Jiang, Y. Wu, and Z.-H. Zhou. Spectral clustering on multiple manifolds. *Neural Networks, IEEE Transactions on*, 22(7):1149–1161, 2011.
- J. Yan and M. Pollefeys. A general framework for motion segmentation: Independent, articulated, rigid, non-rigid, degenerate and nondegenerate. In *ECCV*, volume 4, pages 94–106, 2006.
- A. Y. Yang, S. R. Rao, and Y. Ma. Robust statistical estimation and segmentation of multiple subspaces. In *CVPRW '06: Proceedings of the 2006 Conference on Computer Vision and Pattern Recognition Workshop*, page 99, Washington, DC, USA, 2006. IEEE Computer Society.

- L. Zelnik-Manor and P. Perona. Self-Tuning Spectral Clustering. In *Proceedings of the 18th Annual Conference on Neural Information Processing Systems (NIPS'04)*, 2004.
- T. Zhang, A. Szlam, and G. Lerman. Median K -flats for hybrid linear modeling with many outliers. In *Computer Vision Workshops (ICCV Workshops), 2009 IEEE 12th International Conference on Computer Vision*, pages 234–241, Kyoto, Japan, 2009.
- T. Zhang, A. Szlam, Y. Wang, and G. Lerman. Randomized hybrid linear modeling by local best-fit flats. In *Computer Vision and Pattern Recognition (CVPR), 2010 IEEE Conference on*, pages 1927–1934, 2010.
- T. Zhang, A. Szlam, Y. Wang, and G. Lerman. Hybrid linear modeling via local best-fit flats. *International J. Computer Vision*, 100:217–240, 2012.